Shell Model from a Practitioner's Point of View

Hubert Grawe

Gesellschaft für Schwerionenforschung, Planckstr. 1, 64291 Darmstadt, Germany

Abstract. The lecture presents an introduction to shell model applications in nuclear spectroscopy. The evaluation of single particle energies, two-body interactions and effective operators and their correlation with the choice of model space is described. The results of the empirical shell model approach in a minimum valence space and of large-scale shell model calculations are summarised for various regions in the nuclidic chart. The mapping of the deformed and the spherical shell model is demonstrated, and the evolution of shell structure towards exotic nuclei is discussed.

1 The Nuclear Shell Model

The shell model of the atomic nucleus in its original form [1,2] was founded on the success of the atomic shell model and experimental data of ground state (g.s.) properties such as mass, spin-parity and magnetic moments, which were brought together by merging the assumption of a central potential with the ingenious idea of a spin-orbit force. The progress of the nuclear shell model and its predictive power for excited states and nuclei remote from doubly-magic shell closures is strongly related to its capability to treat many-particle valence configurations. Ever since the pioneering work on the oxygen isotopes [3], and now in its sixth decade, the evolution of shell model calculations is determined by the mutual reinforcement of shell model techniques, computer codes and capabilities on one side, and on the other side experimental developments providing structure data in the exotic areas of the Segré chart far off the stability line. In this lecture the practical aspects of this liaison will be summarized. Thus educated predictions of structure evolution in order to define and design key experiments, and assessment of modern large-scale shell model results should be enforced. Practical "hands-on" formulae and recent key examples will be given to illustrate the power of the nuclear shell model.

The brief introduction into the basics of the nuclear shell model given in this lecture serves as a trigger to more involved studies in textbooks [4, 5], review articles [6,7] and conference proceedings [8]. A more detailed and specialised lecture will be given in a forthcoming lecture in this series [9].

H. Grawe, Shell Model from a Practitioner's Point of View, Lect. Notes Phys. **651**, 33–75 (2004)
http://www.springerlink.com/

1.1 Independent Particle Motion, Nuclear Mean Field Potential and Single Particle Energies

In contrast to the atomic shell model with a spacially well defined central Coulomb potential, in the nuclear shell model the central mean field potential is created by the individual nucleons. Assuming two-body interactions only the nuclear hamiltonian can be formally written as a sum of kinetic (T) and potential (V) energy and rearranged by introducing the one-body nucleon potential U_i.

$$H = T + V = \sum_{i=1}^{A} \frac{\vec{p}_i^{\,2}}{2m_i} + \sum_{i>k=1}^{A} V_{ik}(\vec{r}_i - \vec{r}_k) \tag{1}$$

$$H = \sum_{i=1}^{A} \left[\frac{\vec{p}_i^{\,2}}{2m_i} + U_i(\vec{r}) \right] + \sum_{i>k=1}^{A} V_{ik}(\vec{r}_i - \vec{r}_k) - \sum_{i=1}^{A} U_i(\vec{r}) = H_0 + H_{res} \tag{2}$$

The solutions of a Schrödinger equation with H_0 are the nucleon single particle energies (SPE) in a central potential, as observed in single particle (hole) states outside a doubly-closed shell (CS) nucleus in its neighbours ($CS \pm 1$). The two-body matrix elements (TBME) of the residual interaction H_{Res} represent the mutual interaction of the valence nucleons as observed in the ($CS \pm 2$) neighbours of a magic nucleus. Historically the question whether the introduction of a central potential with independent particle motion is a viable approximation has been discussed controversially in view of the nucleon density and the strength of the nuclear force. The answer was given in the consequent application of the Pauli principle. One may speculate that this discussion has delayed the nuclear shell model by about a decade, as in retrospective the experimental evidence on masses, spins and magnetic moments was known in the mid 1930's [10,11].

In practical applications SPE are obtained from an empirical globally adjusted central potential of e.g. the harmonic oscillator [5], the Woods-Saxon [5] or folded Yukawa [12] type. Alternatively they can be extracted from experimental binding energies (BE) as difference

$$\epsilon_j = BE(CS \pm 1; I = j) - BE(CS; g.s.) \tag{3}$$

where $j \equiv (n, l, j, t_z)$ labels the single particle (hole) ground or excited states in the ($CS \pm 1$) neighbour in radial, orbital and total angular momentum and isospin quantum numbers, which will be itemised only if needed. In this lecture the symbol I will be used for the total angular momentum of a nuclear state, whereas J labels the angular momentum of subgroups of configurations, which for other than two-particle configurations appear in general on the r.h.s. of equations. In (3) BE is used with a negative sign as compared to total binding energies given in mass tables to warrant negative values for bound particles and positive values for hole energies. In Fig. 1 SPE

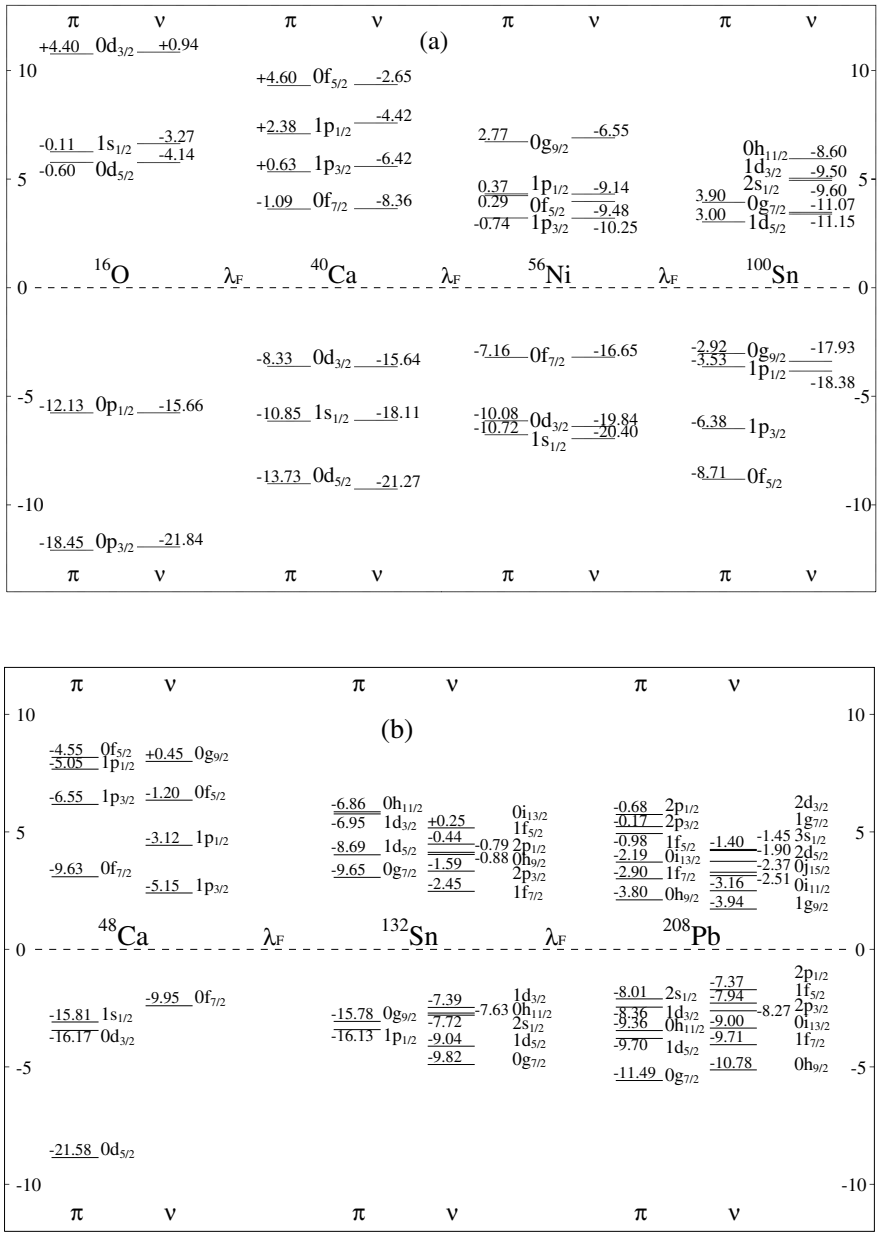

Fig. 1. Experimental single particle (hole) energies for the doubly-magic N=Z ^{16}O, ^{40}Ca, ^{56}Ni, ^{100}Sn (**a**), and the neutron rich ^{48}Ca, ^{132}Sn, ^{208}Pb (**b**). The energies are normalised to the middle of the shell gap (λ_F), which eliminates the Coulomb energy difference ΔE_C. The numbers next to the levels quote the absolute SPE including Coulomb shift

for well established doubly magic nuclei are displayed [13]. As will be shown in Sect. 5 the evolution of SPE is determined by the monopole part V^m of the residual interaction if Coulomb effects are neglected. In the case that SPE are not known for exotic CS nuclei a global fit of V^m to experimental data can be used to infer unknown values [14]. Another global approach to SPE is provided by the mean field Hartree-Fock (HF) method employing schematic interactions [15]. It should be noticed though that SPE determined by different methods are not strictly equivalent:

- a global central potential of a given shape may not account for the realistic nucleon distribution and/or correlations of nucleons at the Fermi surface;
- empirically determined experimental SPE may not exhaust the full spectroscopic strength of the j orbit;
- SPE resulting from mean field models may not account for correlations of e.g. the pairing ($L = 0$), quadrupole ($L = 2$) or octupole ($L = 3$) type, though it is in principle possible to include these modes.

1.2 Empirical, Schematic and Realistic Interactions

With the restriction to two-body interactions the interaction energy (diagonal and non-diagonal) in a many-particle configuration can be reduced to a weighted sum over TBME only (Sect. 2.1). The basic TBME of the residual interaction can be evaluated in three different ways.

Empirical interactions are extracted from experimental data, in the simplest approach, from the binding energies of $CS, CS \pm 1$ and $CS \pm 2$ nuclei. In the case of a single j shell:

$$\langle j^2 J \,|V|\, j^2 J\rangle = BE(CS \pm 2; j^2, I = J) - BE(CS; g.s.) - 2\epsilon_j \qquad (4)$$

with ϵ_j defined in (3), and a straightforward generalisation to non-identical two-particle configurations $(j_1 j_2 J)$ with j_i labelling nucleon orbitals coupled to angular momentum J. Only diagonal TBME can be extracted this way with the consequence that in model spaces with more than one orbit mixing is neglected. Therefore for not too large model spaces the χ^2-fitting method has been applied to determine SPE and TBME (including non-diagonal) from an abundant data set of experimental binding and excitation energies of states that can be assigned to the model space (Sect. 2) [6,16–22]. In the evaluation of TBME it is often convenient to transform from proton-neutron ($\pi\nu$) to isospin representation and vice versa. Except for Coulomb effects the $\pi\pi$ and $\nu\nu$ TBME are identical to $T = 1$ TBME. For $\pi\nu$ TBME the following relation holds:

$$\langle j_1 j_2 J \,|V|\, j_3 j_4 J\rangle_{\pi\nu} = \frac{1}{2}\sqrt{(1+\delta_{j_1 j_2})(1+\delta_{j_3 j_4})} \times (\langle j_1 j_2 J \,|V|\, j_3 j_4 J\rangle_{T=0} + \langle j_1 j_2 J \,|V|\, j_3 j_4 J\rangle_{T=1}) \qquad (5)$$

For conversion of particle-particle to particle-hole TBME see Sect. 2.3.

A χ^2-fitting procedure is greatly simplified by assuming a *schematic interaction* that can be specified by a few parameters. Historically, interactions of the Yukawa [23], Gaussian [23], delta [23] and surface delta [24] types, as detailed in various textbooks [4,5,23], have played a significant rôle in the evolution of shell model calculations. The restrictions and symmetries imposed on the TBME by a given analytic function and radial dependence introduce deficiencies in the energies (pairing, level density) and electromagnetic transition rates (configuration mixing) calculated in the shell model application. Another type of schematic interaction is widely used in mean field calculations employing the HF method (Sect. 1.1), namely the Skyrme [25] and Gogny forces [26]. They have been successfully used to calculate such gross properties as masses, shapes, radii, level densities and single particle energies (Sect. 1.1), but have been scarcely applied to detailed shell model spectroscopy.

Realistic interactions are inferred from experimental nucleon-nucleon (NN) scattering data via effective NN potentials fitted to the data [27–30]. In the standard many-body approach the NN interaction V_{NN} is used to calculate the G-matrix [31–33] which is needed to eliminate the strong repulsive core in V_{NN}. In a second step for a given space of occupied and empty scattering orbitals core polarisation contributions to the TBME are calculated up to a given order of diagrams [33]. The occupied and scattering states are defined by a doubly-magic core serving as reference for the shell model calculation. This method introduces a mass (A) dependence in the extracted TBME, thus requiring a new calculation for every new core nucleus. Though it was never proven rigorously that the procedure converges, the renormalised G-matrix TBME gives an extremely good description of energy levels near closed shells. Unfortunately reliable SPE cannot be obtained in this way and therefore are taken from experiment (Sect. 1.1). Recently a method was developed to eliminate the hard core repulsive (high momentum) contributions to V_{NN} directly [34]. The resulting smooth and non-singular V^{low-k} can then be used to calculate core polarisation corrected TBME carrying no A dependence. Large-scale shell model calculations have revealed that in spite of the excellent results near closed shells realistic interactions fail to reproduce binding energies and the evolution of single particle structure from one closed shell (CS) to the next ($CS \pm 1$). The reason is two-fold:

- experimental SPE are affected by particle-hole (ph) excitations across the closed shell which fade away or change character in moving through the shell;
- a more fundamental deficiency is the neglect of three-body forces as their inclusion is beyond present computational power.

As the evolution of SPE throughout a shell is determined solely by the monopole part of the interaction (Sect. 5), this deficiency can be cured by adding a constant to the diagonal TBME in each multiplet. This correc-

tion has been proven extremely successful in the $(1s, 0d)$ [6,35] and $(1p, 0f)$ shell [7,36].

As a general rule it should be noticed that any effective interaction is valid only for the model space used in its derivation (and if necessary for the truncation scheme employed). Any change in model space and/or truncation requires (and justifies) a renormalisation of the residual interaction.

1.3 Observables and Effective Operators

The diagonalisation of the hamiltonian matrix besides the observable *energy* provides the non-observable *wave function*, which in turn can be used to calculated other observables, such as spectroscopic factors, electromagnetic and β-decay transition rates and static moments [37]. The shell model calculation is optimised to reproduce binding energies and level schemes, which in principle can be achieved with different combinations of interaction and model space (Sect. 3). The corresponding wave functions have generally little overlap and consequently observables probing only specific parts of the wave functions will be calculated with largely deviating values. For example in a single-j proton (or neutron) shell parity changing γ-ray transitions and, not so trivial (Sect. 2.1), $M1$ transitions between states of different seniority are strictly forbidden. Likewise in a single-j proton-neutron shell only a small portion of the Gamow-Teller (GT) strength, the diagonal $l, j \rightarrow l, j$ part, not the dominating $l, j \rightarrow l, j \pm 1$ spin-flip part is different from zero. The general rule is:

What is not in the model space cannot be calculated reliably.

It is obvious from these examples that the effective operators entering calculations of observables other than *energy* are subject to considerable renormalisation depending on the available model space. The most commonly used one-body operators electric quadrupole ($E2$) [4,5,23], magnetic dipole ($M1$) [4,5,23] and Gamow-Teller (GT) [4,5,23,38,39] will be discussed in more detail. The renormalisation is state (orbital) and energy dependent and could be performed in a similar way as for the TBME. This has been demonstrated for the $E2$ operator [40,41]. Alternatively single particle reduced matrix elements of any one-body operator $O^{\sigma L}$ can be fitted by the χ^2 method to experimental data. Similar to the two-body operator (Sects. 1.2 and 2.1) the reduced matrix element of any one-body operator in a many-particle configuration can be decomposed into a sum over single particle matrix elements (see Sect. 2.1 and [4]):

$$\langle I\alpha \left|\left| O^{\sigma L} \right|\right| I'\alpha' \rangle = \sum_{j\alpha j'\alpha'} c_1(l, j, I, \alpha, l'j'I'\alpha') \langle lj \left|\left| O^{\sigma L} \right|\right| l'j' \rangle \qquad (6)$$

After elimination of phase space factors the reduced transition strength is given by:

$$B(O^{\sigma L}; I'\alpha' \to I\alpha) = \frac{1}{2J'+1} \langle I\alpha \left|\left| O^{\sigma L} \right|\right| I'\alpha' \rangle^2 \tag{7}$$

[4,5,23] (see also [38] in this volume). In (6,7) (σL) specify the multipolarity L and the intrinsic parity σ of the operator, (l, j) the orbital and $(I\alpha)$ the state for initial (primed) and final state with α specifying any additional quantum number. The coefficients c_1 are calculated from the amplitudes of the configurations composing the wave functions, by angular momentum recoupling and decoupling single particles from n-particle configurations making use of coefficients of fractional parentage [cfp], which maintain antisymmetrisation as detailed in shell model textbooks [4,5]. This fitting procedure was successfully applied to the $(1s, 0d)$ shell [6]. In many cases it is sufficient to replace the free nucleon coupling constants for protons (π) and neutrons (ν) charge e_π, e_ν for $E2$ [4,5,23], g-factors $g_\pi^L, g_\nu^L, g_\pi^S, g_\nu^S$ for $M1$ [4,5,23] and g_A/g_V for GT [38] by their effective values, which are obtained by an overall fit to experimental values for a given model space. The contributions to the effective operator can be split into a higher-order part, that is constant or weakly dependent on mass A, and a strongly model space dependent part, that can be minimized by choosing an adequate space.

For the $E2$ operator the higher-order (high momentum) term is due to the giant quadrupole resonance, a $\Delta N = 2$ ph-excitation with N specifying the major harmonic oscillator quantum (HO) number [42–44]. It can be expressed as a constant $\delta e_{\pi,\nu}$ added to the free-nucleon values $e_\pi = 1$ e and $e_\nu = 0$. Typical values are $\delta e_{\pi,\nu} \simeq 0.5$ e with a small isovector effect $\delta e_\nu - \delta e_\pi \simeq 0.2$ e [42,43]. In shell model calculations comprising a full major HO shell as $(0p)$, $(1s, 0d)$ and $(1p, 0f)$ this choice of effective charge was found to account well for the experimental data [6,16,45]. In medium-heavy and heavy nuclei it is important to include all pairs of orbitals $(N, l, j \to N, l-2, j-2)$ that are connected by stretched $E2$ transitions having large matrix elements. Such are $(\pi\nu f_{7/2} \to p_{3/2})$ at ^{56}Ni, $(\pi\nu g_{9/2} \to d_{5/2})$ at ^{100}Sn, $(\nu h_{11/2} \to f_{7/2})$ and $(\pi g_{9/2} \to d_{5/2})$ at ^{132}Sn and $(\nu i_{13/2} \to g_{9/2})$ and $(\pi h_{11/2} \to f_{7/2})$ at ^{208}Pb. If this due to truncation is not possible large polarisation charges $\delta e \geq 1.0$ e are needed (Sect. 3.4).

The $M1$ and GT operators can be treated on the same footing as, apart from the differing isospin part and the coupling constant, the GT operator $g_A/g_V(\sigma \cdot \tau)$ is proportional to the spin part of the $M1$ operator [38,46]. In this case the higher-order term of the renormalisation is due to second order tensor correlations and admixtures from the Δ resonance [6,45,46] and amounts to an overall quenching factor $g_{eff}^S/g_{free}^S \simeq 0.7$ of the spin operator [46] and correspondingly for g_A/g_V [45]. For the $M1$ operator the orbital g-factor g^L is changed by adding $\delta g^L \simeq \pm 0.1$ to the neutron and proton free nucleon values $g^L = 0, 1$, respectively [46–48]. To minimize the strongly

model space dependent part of the renormalisation it is mandatory to include all $0\hbar\omega$ spin-orbit partners in the model space.

In Sect. 3 typical examples for renormalised coupling constants will be given for minimum and extended model spaces. Effective charges are also discussed in Sect. 3.3 of [49] in this volume. Quenching factors for the GT strength are given in Sect. 6.1 of [38] in this volume.

For electromagnetic transitions, besides natural units [as defined by the coupling constant and radial dependence of the operator $O^{\sigma L}$ in (7), namely $[e^2 fm^{2L}]$ and $[\mu_N^2 fm^{2L-2}]$ for electric (EL) and magnetic (ML) transitions, respectively], relative so-called Weisskopf units [*W.u.*] are used. They are based on an estimate for the single-proton strength [5,50,51] and defined as:

$$B_{W.u.}(EL) = \frac{1}{4\pi}\left(\frac{3}{L+3}\right)^2 R^{2L} e^2 fm^{2L} \tag{8}$$

and

$$B_{W.u.}(ML) = \frac{10}{\pi}\left(\frac{3}{L+3}\right)^2 R^{2L-2} \mu_N^2 fm^{2L-2} \tag{9}$$

with the nuclear mean radius $R = 1.2 \cdot A^{1/3} fm$, the elementary charge e and the nuclear magneton μ_N. For definition of $B(GT)$ see [38] in this volume.

1.4 Model Space, Truncation, Codes

In the previous sections the importance of choosing an appropriate model space was emphasized. In practice, "no-core" shell model calculations in many harmonic oscillator shells involving up to 5 $\hbar\omega$ (A=12) resp. 50 $\hbar\omega$ (A=4) can be performed only in light nuclei (A$\leq$12) [52,53] with the unrenormalised G-matrix. For heavier systems an inert core has to be assumed and effective residual interactions and operators as described in Sects. 1.2 and 1.3 have to be employed. With modern shell model codes untruncated calculations within in one HO shell can be performed for the $0p$ ($N = 1$,$^4\underline{\mathrm{He} - {}^{16}\mathrm{O}}$), $1s, 0d$ ($N = 2$,$\underline{{}^{16}\mathrm{O} - {}^{40}\mathrm{Ca}}$) and $1p, 0f$ ($N = 3$,$\underline{{}^{40}\mathrm{Ca} - {}^{60}\mathrm{Zn}}$) shell. Inclusion of ph excitations around shell closures and of intruder orbitals in jj major shells with Z,N$\geq$28 require truncation. This can be achieved in various ways:

- restriction of the number of shell model orbitals, sometimes called *vertical* truncation;
- restriction of the ocupation number within a given set of single particle orbits (*horizontal* truncation), which in high-j orbitals is often achieved by seniority truncation [54] (Sects. 2.1 and 3.6);
- restriction according to importance of a configuration, e.g. by excluding components with the least bound diagonal matrix elements from the diagonalisation [40] or by probing importance by Monte Carlo sampling [55].

The number of shell model codes developed in the past is abundant and their power and capability is a true mirror of the progress in computer technology. Only a few standard codes will be listed here to demonstrate the evolution and state of the art in shell model calculations. Based on the many-particle shell model theory exploiting Racah algebra and second quantisation as developed in the early 1960's [56] the first codes were coupled ones maintaining good angular momentum. A highly developed representative of this class is RITSCHIL [57] which is still in use [58,59]. With increasing dimension the number of non-zero hamiltonian matrix elements explodes and eventually exceeds the limits of storage capabilities. In parallel, in the late 1970's the superior storage capabilities of m-scheme Slater determinants were exploited to overcome this problem [60]. This development produced the widely used code OXBASH [61] and culminated in ANTOINE [62,63] taking advantage of the enormous progress in computer performance. Both codes, including a variety of interactions in various model spaces are open for use and well documented. The examples listed in Sect. 3 were mainly obtained with these codes. Comparable efficiency is known to be achieved by the codes MSHELL [64] and VECSSE [65]. The m-scheme reaches its limits with increasing dimension, which is substantially larger than in a coupled code. Therefore the presently most powerful code NATHAN [62,63] uses angular momentum coupling again. The present dimensional limitation is thus reached in the middle of the $1p, 0f$ shell at ^{60}Zn with $2.0 \cdot 10^9$ $m = 0$ configurations [66,67].

2 Empirical Shell Model

In the past the empirical shell model (ESM) has been frequently used to interprete experimental data close to doubly closed (sub)shells, to extrapolate features of nuclear structure within and between adjacent major shells and to even make spin-parity and configuration assignments to states in exotic nuclei [69–73]. The ESM is characterized by the following features:

- minimum model space, i.e. single j-shell, low-j subshells or few-particle configurations;
- single particle energies (SPE) and two-body matrix elements (TBME) from experimental interaction energies;
- no configuration mixing.

The latter restriction is released in small low-j model spaces as e.g. $\pi\nu(0p)$ (22 TBME, 4 SPE) [16], $\pi\nu(1s0d)$ (78 TBME, 6 SPE) [6], $\pi\nu$ $(0f_{7/2})$ (16 TBME, 2 SPE) [17], or $\pi\nu(1p_{1/2}, 0g_{9/2})$ (26 TBME, 4 SPE) [18–20], where a free fit of the shell model parameters including non-diagonal TBME to experimental data is possible. The present limit of this method has been reached with the $\pi\nu(1p, 0f)$ model space comprising 195 TBME and 8 SPE [21,22]. Assuming two-body forces the interaction energy (hamiltonian matrix element) within and between any configuration is given by a sum over all possible TBME weighted by coefficients involving angular momentum coupling

coefficients and coefficients of fractional parentage, which decouple the two-particle wave functions from the remaining nucleons in the configuration [4,5, 56] maintaining antisymmetrisation. This is accomplished by Racah algebra and is outlined in various textbooks where also useful formulae for practical application are given [4,5,51]. The interaction of the valence particles with the inert core is accounted for by adding their single particle energies, representing the independent particle solutions of H_0 in (2) of Sect. 1.1, to the diagonal interaction.

In spite of its simplicity the ESM has been very successful in predicting excitation and even binding energies. On the other hand the limited model space and the neglect of configuration mixing have the consequence that the wave functions have only marginal overlap with the "true" wave functions, as e.g. the solutions of large-scale shell model (LSSM) calculations. Consequently transition rates are reproduced only at the expense of largely renormalised single particle operators for allowed transitions, and weak or forbidden transitions often cannot be described at all (Sect. 1.3). In the following examples the simplicity and limitations of the ESM approach will be outlined.

2.1 Seniority in $\mathbf{j^n}$ Configurations

In a single-j shell configuration the methods outlined above result in this expression for interaction energies:

$$\langle j^n \alpha I \,|V|\, j^n \alpha' I\rangle = n\epsilon_j \delta_{\alpha\alpha'} + \sum_{J'} c_2(n, j, I, \alpha, \alpha', J') \langle j^2 J' \,|V|\, j^2 J'\rangle \quad (10)$$

i.e. the matrix element is completely determined by the one- and two- particle (hole) neighbours of the doubly-magic core nucleus yielding the SPE ϵ_j and the TBME $\langle j^2 J' \,|V|\, j^2 J'\rangle$. If one is not interested in total binding energies the SPE can be ignored and the TBME can be replaced by the j^2 excitation energies in the two-particle (hole) neighbour nucleus. Additional quantum numbers α are needed to distinguish between different Slater determinants with identical spin I. The coefficients $c_2(n, j, I, \alpha, \alpha', J')$ are tabulated in the literature [74]. For $j > 7/2$ the most important additional quantum number is the seniority v which counts the number of nucleons not coupled to $J' = 0$ pairs. Seniority imposes a few symmetry rules that can favourably be exploited in nuclear structure applications [4,51].

- Excitation energies are independent of shell occupation n.
- Matrix-elements of even-tensor one- and two-particle operators change sign in midshell, i.e. they vanish for $n = (2j + 1)/2$.
- Odd-tensor one- and two-particle operators are diagonal in seniority.

It was shown that δ-interactions are odd-tensors [4], which in view of the short-range nature of the nucleon-nucleon interaction stresses the importance

of seniority conservation for nuclear structure calculations. This is frequently exploited for truncation schemes in shell model codes (Sects. 1.4 and 3.6). As a consequence of these symmetries for one-body operators and fixed seniority v (6) simplifies to [4]

$$\langle j^n v I \,||O^{\sigma L}||\, j^n v I' \rangle = \frac{2j+1-2n}{2j+1-2v} \langle j^v I \,||O^{\sigma L}||\, j^v I' \rangle;\ L = even \quad (11)$$

$$= \langle j^v I \,||O^{\sigma L}||\, j^v I' \rangle;\ L = odd \quad (12)$$

and with the help of tabulated [cfp] for $v \geq 3$ and [cfp]$\equiv 1$, $J_1 = j$ for $v = 2$

$$\langle j^v v I \,||O^{\sigma L}||\, j^v v I' \rangle = v \sum_{J_1} [j^v I\{|j^{v-1} J_1) j I][j^{v-1} J_1\{|j^v I') j I'](-1)^{J_1+j+I+L}$$

$$\times \sqrt{(2I+1)(2I'+1)} \begin{Bmatrix} j & I & J_1 \\ I' & j & L \end{Bmatrix} \langle lj \,||O^{\sigma L}||\, lj \rangle \quad (13)$$

Equation (13) is generalised to n particles by replacing v with n and introducing additional quantum numbers v, α in initial (I'), final (I) and ($n-1$) state (J_1) [4]. As also all transition matrix elements and moments are proportional to the same single particle matrix element $\langle lj \,||O^{\sigma L}||\, lj \rangle$ for a given nucleus they are related by factors depending on (v, I, I', L) only. This has been exploited in the past to relate seniority isomers (v, I_{max}) $B(E2; I_{max} \rightarrow I_{max} - 2)$ to quadrupole moments $Q(v, I_{max})$ in order to calibrate the quadrupole coupling constants in hyperfine experiments [37,75]. For a fixed j and seniority v the maximum configuration spin is given by $I_{max} = v(j - (v-1)/2)$.

In Fig. 2 features of the seniority scheme are demonstrated for the N=50 isotones between ^{90}Zr and ^{100}Sn. The proton model space is $\pi(1p_{1/2}, 0g_{9/2})$ (see Fig. 1) and the SPE and TBME are taken from one of the numerous fits to experimental data [19] (see also [18,20]). The additional $p_{1/2}$ orbit introduces only a small distortion of the pure $g_{9/2}$ seniority scheme, nevertheless all empirical interactions in this model space are seniority conserving [18–20]. In Fig. 2a the experimental and ESM levels are shown for lowest seniority $v = 2, 3$, respectively, and selected $v + 2$ states. The constancy of excitation energies with identical v is clearly visible. Only the $v = 0$ ground state is lowered with increasing distance from the doubly-magic ^{100}Sn due to pair scattering from the $p_{1/2}$ and the $f_{5/2}, p_{3/2}$ orbitals, which latter are from outside the model space. It is obvious that this effect is partly accounted for as the TBME fit included mainly nuclei in the lower $\pi g_{9/2}$ shell since the heavier isotones were not known at the time when the fit was made. This also explains the increase in level deviations from ^{92}Mo to ^{98}Cd (see Sect. 3). Readjustment of SPE and TBME with the knowledge of the exotic isotones results in a greatly improved overall agreement [76]. In Fig. 2b the even-tensor $E2$ transition strengths $B^{1/2}(E2)$ are shown for transitions $I_{max}, v \rightarrow I_{max} - 2, v'$ for $|v - v'| = \Delta v = 0, 2$. Besides the ESM results the pure $g^n_{9/2}$ values according

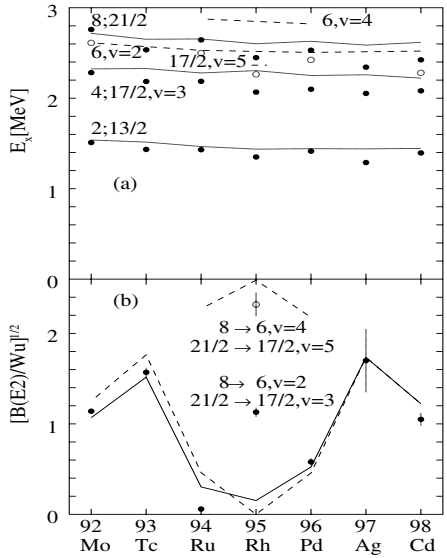

Fig. 2. Experimental (•,○) and ESM (lines) lowest-seniority $v = 2, 3$ and selected $v + 2$ levels for even- and odd-A N=50 isotones ^{92}Mo to ^{98}Cd (**a**) and E2 strengths $B^{1/2}(E2; I_{max} \rightarrow I_{max} - 2)$ with $\Delta v = 0, 2$ (**b**). Open symbols refer to dashed lines

to (11) are given, too. An effective $E2$ charge $e_\pi = 1.52\ e$ is used, which fits best the experimental data. The symmetry around midshell is distorted due to a $p_{1/2}$ pair scattered to $g_{9/2}$ giving rise to premature filling of the orbit. The discrepancy for the midshell nucleus ^{95}Rh is worth mentioning. As for the half-filled shell the $21/2^+, v = 3 \rightarrow 17/2^+, v = 3$ should be small or zero, one would expect only a strong $21/2^+, v = 3 \rightarrow 17/2^+, v = 5$ transition (see level scheme Fig. 2a). Experimentally, however, both branches are observed with comparable strengths (Fig. 2b). This cannot be explained by mixing within the model space as due to the seniority conserving interaction odd- and even-tensor two-body matrix elements vanish in midshell (see symmetry rules above and [71]). Therefore core excitation beyond the present model space is the only possible reason. Indeed this was proven recently in large-scale shell model calculations in the (gds) model space and interaction [77] (Sect. 3.4), yielding values of 0.4 and 4.0 W.u. for the forbidden $\Delta v = 0$ and the allowed $\Delta v = 2$ transitions, respectively.

Finally in none of the N=50 isotones above ^{90}Zr a $\Delta v = 2$ $M1$ odd-tensor transition is observed experimentally between states in the minimum model space [78]. This nicely demonstrates the symmetry relations listed above.

As another example $\nu g^n_{9/2}$ states in Ni isotopes beyond N=40 are shown in Fig. 3a. Single particle energy and the $\nu g^2_{9/2}$ TBME are extracted from binding [79] resp. excitation [80] energies in ^{68,69,70}Ni assuming ^{68}Ni to be a reasonable core nucleus (see Sects. 3.3 and 5.3 for further discussion). They

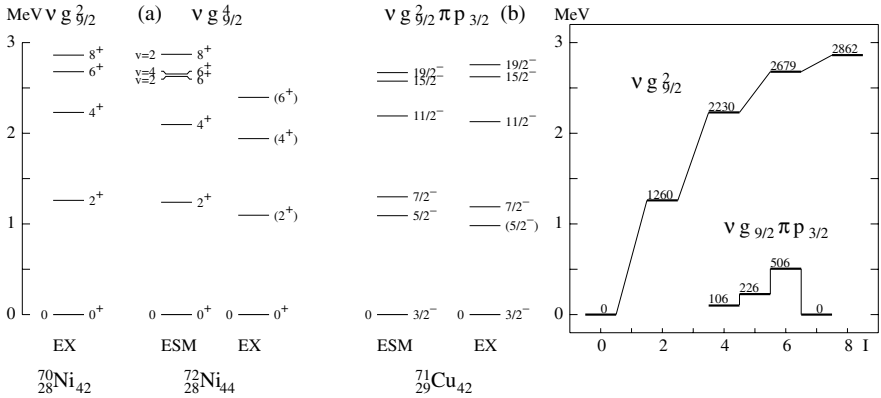

Fig. 3. Experimental and ESM level schemes for ^{72}Ni (**a**) and ^{71}Cu employing the empirical TBME shown in (**b**)

are shown in Fig. 3b with their absolute values, which slightly differ from those given in [70] due to updated input data. The results for ^{72}Ni show a striking difference as compared to the valence mirror N=50 isotones (Fig. 2). The seniority $v = 4$, 6^+ state is predicted below the 8^+ allowing for a fast $B(E2)$ which destroys the isomerism observed in ^{70}Ni [80,81] and in the valence mirror ^{94}Ru (Fig. 2). This difference can be traced back to the $J = 2$ TBME, which is more strongly bound and enters the $v = 4$ interaction energies in (10) with a large weight $c_2(4, 9/2, 6, v = 4, 2)$ [74]. The experimental data from a recent β-decay experiment shown in Fig. 3a support this scenario based on the seniority scheme [80].

Further examples for the seniority scheme in largely isolated j^n shells can be found in the $\pi\nu f_{7/2}$ [17], $\nu h_{11/2}$, Z=50 [82], $\pi h_{11/2}$, N=82 [83] and $\pi h_{9/2}$, N=126 [84] nuclei.

2.2 Three and More Particles in Non-equivalent Orbitals

For particles in non-equivalent orbitals (10) is modified and the general case of configurations $j_1^{n_1} j_2^{n_2}$ treated in the literature [4] will be exemplified in the following for $n_1, n_2 = 1, 2$. The interaction of a nucleon j_2 with a configuration j_1^n is given by

$$\langle j_1^n(\alpha_1 J_1) j_2 I \,|V|\, j_1^n(\alpha_1' J_1') j_2 I\rangle = n \sum_{\alpha_{11} J_{11}} [j_1^n \alpha_1 J_1 \{|j_1^{n-1}(\alpha_{11} J_{11}) j_1 J_1]$$

$$\times [j_1^{n-1}(\alpha_{11} J_{11}) j_1 J_1' |\} j_1^n \alpha_1' J_1'] \sqrt{(2J_1+1)(2J_1'+1)} \sum_{J'} (2J'+1) \begin{Bmatrix} J_{11} & j_1 & J_1 \\ j_2 & I & J' \end{Bmatrix}$$

$$\times \begin{Bmatrix} J_{11} & j_1 & J_1' \\ j_2 & I & J' \end{Bmatrix} \langle j_1 j_2 J' \,|V|\, j_1 j_2 J'\rangle \qquad (14)$$

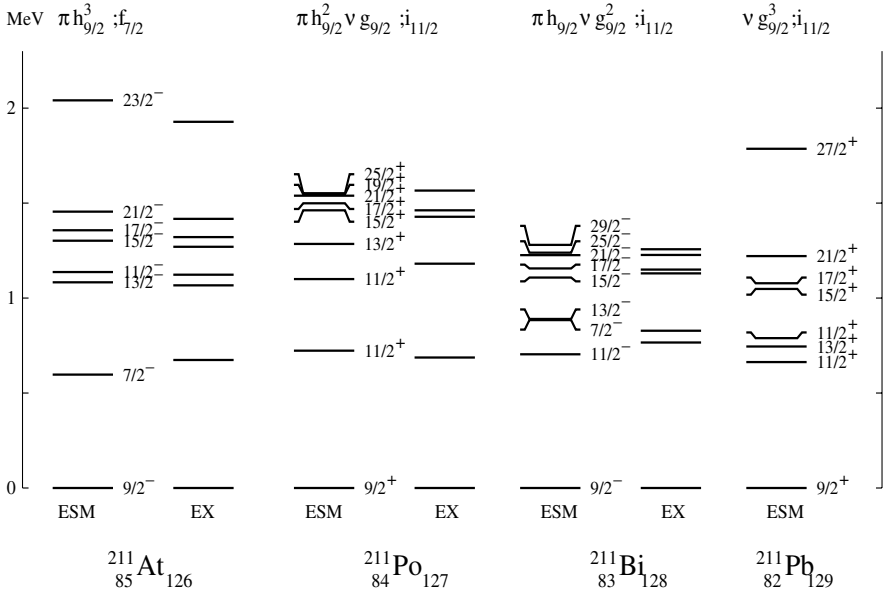

Fig. 4. Experimental and ESM level schemes for the A=211 isobars of the elements At, Po, Bi and Pb

where the $[cfp] \equiv 1$ for $n = 2$. For the total interaction energy (diagonal matrix elements) the SPE and the j_1^n energy c.f. (10) have to be added. In Fig. 3b ESM results c.f. (14) for ^{71}Cu in the configuration $\pi p_{3/2}\nu g_{9/2}^2$ using the TBME as deduced from ^{70}Ni and ^{70}Cu [70] are compared to experiment yielding excellent agreement. In Fig. 4 ESM predictions for the three-particle A=211 isobars of At, Po, Bi and Pb with dominant configurations $\pi h_{9/2}^n \nu g_{9/2}^{3-n}$, n =Z-82 are shown and found to provide good predictive power for the experimentally poorly known ^{211}Pb. The predicted $M3$ isomerism awaits experimental verification. The ESM model space includes also the $\pi f_{7/2}$ and $\nu i_{11/2}$ orbits which prove to be essential for the high-spin states.

For more than two active orbitals the mutual interaction can be reduced to interaction energies between all combinations of two orbitals, as e.g. for three groups

$$\langle (J_1 J_2) J', J_3; I \,|V|\, (J_1 J_2) J, J_3; I \rangle = \sum_{J_{13}} (-1)^{J'+J} \sqrt{(2J'+1)(2J+1)}$$
$$\times (2J_{13}+1) \begin{Bmatrix} J_1 & J_2 & J' \\ I & J_3 & J_{13} \end{Bmatrix} \begin{Bmatrix} J_1 & J_2 & J \\ I & J_3 & J_{13} \end{Bmatrix} V(J_1 J_3 J_{13}) + \sum_{J_{23}} \sqrt{(2J'+1)(2J+1)}$$
$$\times (2J_{23}+1) \begin{Bmatrix} J_2 & J_1 & J' \\ I & J_3 & J_{23} \end{Bmatrix} \begin{Bmatrix} J_2 & J_1 & J \\ I & J_3 & J_{23} \end{Bmatrix} V(J_2 J_3 J_{23}) + \delta_{JJ'} V(J_1 J_2 J) \quad (15)$$

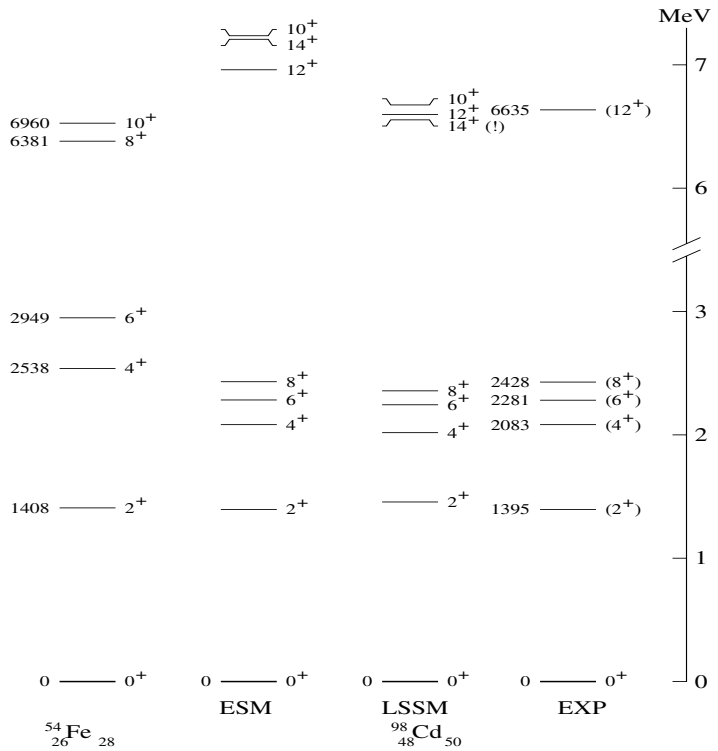

Fig. 5. Core excited isomers in ^{54}Fe (experiment) and one major shell higher in ^{98}Cd as predicted by ESM. For comparison LSSM results in the (*gds*) space are given, too (Sect. 3.4). Between 3 and 6 MeV the energy scale is cut by 2 MeV

with short notations J_i for groups of n_i particles in orbit j_i and $V(J_iJ_kJ_{ik}) = \langle j_i^{n_i}\alpha_iJ_i\ j_k^{n_k}\alpha_kJ_kJ_{ik}\,|V|\,r.h.s.\rangle$. If angular momentum coupling allows more than one J value a diagonalisation is required. For $n_1 = n_2 = n_3 = 1$ and stretched coupling to maximum spin J and I the r.h.s. of (15) becomes the sum of the three maximum spin TBME $V(j_1j_2(j_1+j_2)) + V(j_1j_3(j_1+j_3)) + V(j_2j_3(j_2+j_3))$.

To demonstrate the predictive option towards exotic nuclei in Fig. 5 the two-proton hole nuclei in ^{56}Ni and ^{100}Sn, ^{54}Fe and ^{98}Cd, are compared in ESM predictions for core excited isomers. The respective configurations are $\pi f_{7/2}^{-2}\nu f_{7/2}^{-1}p_{3/2}$ and $\pi g_{9/2}^{-2}\nu g_{9/2}^{-1}d_{5/2}$ which differ by one major shell (Fig. 1). Clearly the known I^π=10$^+$ isomer in ^{54}Fe has its I^π=12$^+$ counterpart in ^{98}Cd, which was identified recently [85]. The TBME for ^{98}Cd are taken from ^{90}Nb for $\pi g_{9/2}\nu g_{9/2}^{-1}$, ^{92}Nb for $\pi g_{9/2}\nu d_{5/2}$, ^{90}Zr for $\nu g_{9/2}^{-1}d_{5/2}$ and ^{98}Cd for $\pi g_{9/2}^2$. Experimental *ph* TBME were converted to *pp* by using (16) (Sect. 2.3).

2.3 Particle-Hole Conjugation

The symmetry of level energies and transition strengths with respect to the middle of a single j shell, i.e. the equivalence of particles (p) and holes (h) is demonstrated in Sect. 2.1 and Fig. 2. In spectroscopy application this provides a sound extrapolation from known regions close to stability to exotic nuclei, as e.g. from ^{92}Mo to ^{98}Cd in Fig. 2. The equivalence of pp and hh interactions, i.e. except for single particle (hole) energies due to different core nuclei, holds also for configurations of non-equivalent nucleons and orbitals. For different ph character of the nucleons the ph and pp (or the identical hh) TBME are related by [4,51]

$$\langle j_1 j_2 J\,|V|\,j_3 j_4 J\rangle = -\sum_{J'}(2J'+1)\begin{Bmatrix} j_4 & j_3 & J \\ j_2 & j_1 & J' \end{Bmatrix}\langle j_2 j_3^{-1} J'\,|V|\,j_4 j_1^{-1} J'\rangle + C \quad (16)$$

The additive constant C is given by the monopole part of the $j_1 j_2$ interaction (see Sect. 5) and can be absorbed in modified single particle (hole) energies. The swapping of the coupling sequence is of no concern for diagonal TBME, for non-diagonal it should be remembered that $|j_1 j_2\rangle = (-)^{j_1-j_2}|j_2 j_1\rangle$. In Fig. 6a the ph transformation is shown for the $\pi g_{9/2}\nu d_{5/2}$ pp multiplet in ^{92}Nb towards the ph nucleus ^{96}Nb. The excellent agreement with the experimental ^{96}Nb levels proves the doubly-magic features of both ^{90,96}Zr at Z=40, N=50 and N=56, respectively. Note that in this configuration the levels in ^{100}In

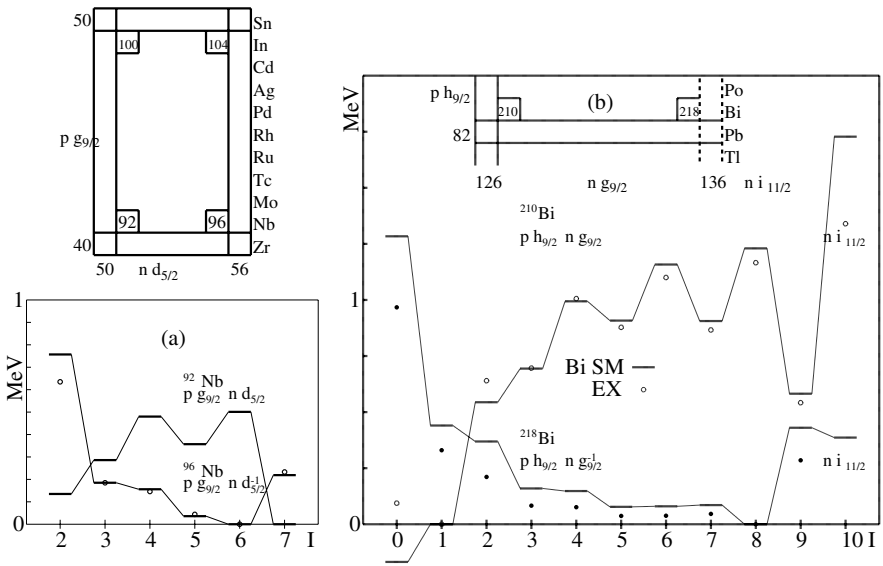

Fig. 6. Particle-hole conjugated spectra for ^{92,96}Nb $\pi g_{9/2}\nu d_{5/2}$ (**a**) and ^{210,218}Bi $\pi h_{9/2}\nu g_{9/2}$ (**b**). The full points in ^{218}Bi result from ph transformation of experimental ^{210}Bi levels

(ph) and ^{104}In (hh) should be identical to ^{96}Nb (ph) and ^{92}Nb ($pp \equiv hh$), respectively. This is not observed in experiment as the neutron $d_{5/2}$ orbit, energetically isolated at Z=40, is highly distorted by the almost degenerate $g_{7/2}$ at Z=50 (see Figs. 1 and 16d). In Fig. 6b the predictive power of the ph transformation is exploited for the $\pi h_{9/2}\nu g_{9/2}$ multiplet beyond ^{208}Pb. The ^{210}Bi pp multiplet translates into the largely unknown exotic ^{218}Bi ph spectrum, assuming the $\pi h_{9/2}$ and $\nu g_{9/2}$ orbits to be undistorted by the neighbouring $\pi f_{7/2}$ and $\nu i_{11/2}$ subshells. Experimentally the ground state of ^{218}Bi was suggested recently to have $I^\pi = (8^-)$ in agreement with the prediction [86].

Single particle matrix elements of one-body irreducible tensor operators of rank L under particle-hole conjugation reproduce themselves up to a phase factor

$$\langle j^{-1} \left|\left| O^{\sigma L} \right|\right| j'^{-1} \rangle = (-)^{L+1} \langle j \left|\left| O^{\sigma L} \right|\right| j' \rangle \tag{17}$$

c.f. (11,12) for the special case $j = j', v = 1$ and $n = 1, 2j$, respectively.

While the examples presented so far require only little computational effort, it is advisable in more complicated configurations to make use of handy standard codes such as e.g. OXBASH (Sect. 1.4).

3 Shell Model Applications

Nuclear shell model calculations have been performed in a large number of systems throughout the Segré chart. Starting from the early empirical approach (ESM) (Sect. 2) and restriction to the close neighbours of doubly-magic nuclei untruncated calculations are now possible within one major HO shell for $N = 1-3$ up to A=70. This enables for the first time the decoupling of the truncation and the interaction problems. For the upper part of the $N = 3$ and any higher shell restrictive truncation is mandatory even close to magic numbers as the highest-spin intruder orbital from the $N + 1$ shell has to be included due to the increasing spin-orbit splitting. This raises the problem of spurious states; $I^\pi = 1^-$ states arising from the center of mass motion of the nucleus without any structural relevance. It affects of course every calculation at the borderline of two adjacent HO shells even in light nuclei. Another problem arises from the fact that realistic interactions valid for two adjacent HO shells cannot be derived reliably. This has hampered the predictive power of the shell model especially for the evolution of shell structure. In this section a few examples for success and failure of shell model results, mainly for exotic nuclei across the Segré chart, will be discussed to demonstrate the present status of the spherical shell model approach.

The accuracy of a shell model calculation is difficult to assess, as it is a complex mixture of systematic uncertainties due to model space, truncation and interaction used. In case of fitted SPE and TBME the statistical uncertainties play a significant rôle, too. As a measure for the agreement

of experiment and theory very often the mean level deviation (MLD) is used [19]:

$$MLD = \left[\frac{1}{n}\sum_{i}^{n}(E_i^{EX} - E_i^{SM})^2\right]^{1/2} \tag{18}$$

where n is the number of states compared. In the fitting procedure of TBME MLD is replaced by a proper χ^2 considering degrees of freedom and statistical weight of the addends [19]. As example for the spectra shown in Fig. 2 the MLD values for ^{92}Mo, which was included in the TBME fit, and ^{98}Cd, which was unknown at the time of the fit, are 35 keV and 170 keV, respectively. The numbers change to 80 keV and 150 keV, when SPE and TBME are varied randomly within their uncertainties. Typical MLD values in the $\pi\nu(p_{1/2}, g_{9/2})$ model space are between 100 keV for N=50 and 250 keV for N=47 [87].

3.1 The N=2 (1s,0d) Shell: ^{16}O - ^{40}Ca

Nuclei in this shell are well described with the universal interaction USD as inferred from a fit to experimental data [6]. Results for levels, binding energies, effective $E2, M1$ and GT operators are reviewed in [6]. Even quadrupole degrees of freedom are accounted for (Sect. 4.1). A challenge to the shell model is provided by the experimentally observed shell quenching at the neutron rich N=20 border [88] as discussed in Sects. 4.1 and 5.3 and by the recently established superdeformation in ^{36}Ar [89]. Both phenomena require consistent inclusion of the $(1p, 0f)$ orbitals in model space and interaction [22].

3.2 The N=3 (1p,0f) Shell: ^{40}Ca - ^{48}Ca - ^{56}Ni

With modern codes like ANTOINE and NATHAN (Sect. 1.4) nearly or fully untruncated shell model calculations can be performed up to ^{60}Zn, where the maximum number of configurations is reached. A number of interactions could therefore be derived and adjusted for this model space, the most commonly used are KB3 [7,36], FPD6 [21] and more recently GXPF1 [22], the latter, however, derived by use of the Monte Carlo shell model method [90]. Interactions of the KB3 family are based on a realistic G-matrix [31] with a proper monopole correction that, starting from ^{40}Ca, transports the single particle energies and shell gaps to ^{48}Ca and ^{56}Ni. The pure and uncorrected G-matrix would produce a collapse of the N=28 gap in ^{48}Ca and a deformed g.s. in ^{56}Ni independently of the specific type of NN potential [63]. The FPD6 and GXPF1 interactions are fits of the 195 TBME and 4 SPE to experimental data. Because of the large number of parameters either a model interaction, e.g. a G-matrix, is used as a starting point (FPD6) [21] or linear combinations

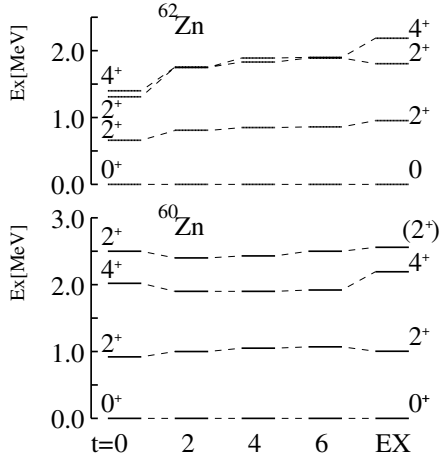

Fig. 7. Convergence of the LSSM results for low-spin states in ^{60,62}Zn with truncation level t (number of *ph* excitations across ^{56}Ni) [66]

of TBME are fitted (GXPF1) [22] to avoid ambiguities in badly determined TBME values. In the lower shell between ^{40}Ca and ^{56}Ni excellent agreement with experiment is achieved for levels, electromagnetic and GT transition rates [36,45,91–93]. Especially the mid $f_{7/2}$ quadrupole deformation phenomena including band crossing are well accounted for (Sect. 4.2). The accuracy of the wave functions has reached a level where Coulomb energy differences (CED) in $T = 1/2$ mirror nuclei [94] and $T = 1$ isobars [95] can be analysed. The application of LSSM wave functions as a spectroscopic tool yields configuration assignments to rotational bands, band crossings [94] and radius information for individual high-spin states [96]. Besides electromagnetic properties GT decay rates and distributions [36,45,93] are well described using effective operators as discussed in Sect. 1.3. The importance of firm GT distribution and strength predictions for astrophysical nuclear synthesis network calculations is discussed in Sects. 4.1 (Fig. 5) and 6.2 (Fig. 12) of [97] in this book.

The jj coupling doubly magic ^{56}Ni has been studied in detailed LSSM calculations [77,98]. Its g.s. was found to be closed shell to 50 - 65%. The convergence of the shell model results with increasing number t of *ph* excitations included (t = truncation level) has been investigated yielding convergence for the $I^\pi = 2^+$ excitation energy at t=7-8. Other properties like $B(E2)$ values, definitely in nuclei with valence nucleons outside the ^{56}Ni core seem to converge faster. Examples for Ni isotopes are shown in Fig. 11 in comparison to ^{100}Sn, one major shell higher [77]. In Fig. 7 the convergence for low-lying states in ^{60,62}Zn is shown [66], the $(1p, 0f)$ nuclei involving the maximum number of configurations at t=16 with respect to ^{56}Ni. Clearly at t=6 convergence is already reached.

As in the $N = 2$ HO shell (Sects. 3.1 and 4.1), a deformed $4p4h$ band in ^{56}Ni found experimentally [99,100] is reproduced in LSSM calculations [101, 99], whereas superdeformed bands require full account is taken of the $g_{9/2}$ orbital which is still beyond present computing capabilities.

3.3 The N=3 Plus Intruder Shell: ^{48}Ca - ^{56}Ni - ^{78}Ni

Due to the weak Z,N=40 HO shell, a consequence of the increasing spin-orbit splitting, shell model calculations in the upper $(1p, 0f)$ shell require inclusion of the $N = 4$ intruder $0g_{9/2}$. At N=Z, where protons and neutrons have to be treated on the same footing, truncation limits meaningful shell model calculations to ^{64}Ge at N=Z=32 well below the region of coexisting deformed shapes at N,Z=36-40. Therefore the following discussion will be restricted to stable and neutron-rich nuclei beyond N=28 in the triangle ^{48}Ca - ^{56}Ni - ^{78}Ni, where the $\nu f_{7/2}$ orbit can be regarded as filled. Extension of the standard (p, f) interactions as KB3 to the $g_{9/2}$ orbit are hampered by the fact that monopole corrections are ambiguous since single particle/hole states around ^{78}Ni are not known. Calculations are essentially limited to the semi-magic Ca and Ni isotopes and the N=28 isotones and their closest neighbours. Key topics in this region are the weakness and disappearance of the N=40 shell around ^{68}Ni, appearance of a new N=32,34 closure in Ca isotopes, which will be discussed in detail in Sect. 5, and the persistence of the N=50 shell in ^{78}Ni [80,102–104]. It is worth mentioning here that different interactions as e.g. KB3, FPD6 and GXPF1 give different answers to these topics [105]. In Fig. 8 the excitation energies and $B(E2; 2^+ \rightarrow 0^+)$ transition strengths in the Ni isotopes are compared to shell model calculations [106, 107]. At N=40 a large E_{2^+} and a small $B(E2)$ indicate a shell closure at ^{68}Ni. The one- and two-particle neighbours can be described in simple shell model configurations [70,108,109], while the hole neighbours cannot [110,111] (Sect. 5.3). The 2n separation energies S_{2n} do not show any shell effect at N=40 [109]. The explanation for the apparent shell closure is two-fold: (i) the parity change from the (p, f) to the $g_{9/2}$ orbit requires an $2p2h$ excitation to build a 2^+ state , which cannot decay back to the g.s. due to particle forbiddance for the one-body $E2$ operator [109]; (ii) shell model calculations in the full $\nu(1p, 0f_{5/2}, 0g_{9/2})$ space show that $L = 0$ pair scattering across N=40 is responsible for the missing effect in S_{2n} [106] as shown in the upper panel of Fig. 8 (see also Sect. 3.6). The rôle of this weakening of the N=40 shell for modelling astrophysical core collapse supernovae is stressed in Sect. 6.3 of [97]. Recently it was shown that there is a large $E2$ strength in ^{68}Ni above 4 MeV [112] in agreement with earlier mean field results [113]. This excludes existence of a substantial (sub)shell closure. On the other hand the small E_{2^+} and large $B(E2)$ to the g.s. in Zn and Fe isotopes are well accounted for in LSSM calculations [107,114]. The shell driving mechanism causing the evolution of deformation around ^{66}Fe is discussed in Sect. 5.3. As $L = 0$ pair scattering preserves seniority (Sect. 3.6), I^π=8^+ isomers should be observed

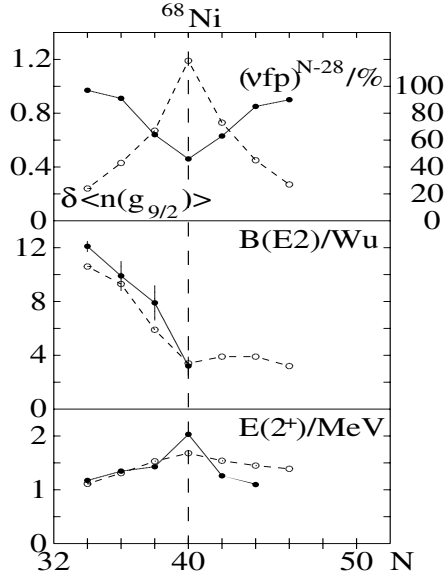

Fig. 8. Experimental and LSSM $I^\pi = 2^+$ excitation energies and $B(E2; 2^+ \to 0^+)$ values for Ni isotopes [106,107]. The upper panel shows the number of excessive $g_{9/2}$ neutrons and the total partition of fp neutrons. The peak (dip) at ^{68}Ni indicates pair scattering across N=40

in the $0g_{9/2}$ shell beyond N=40. They were identified in ^{70}Ni [81] and ^{76}Ni [102], but in contrast to the N=50 valence mirror nuclei ^{92}Mo - ^{98}Cd (Fig. 2) their existence can be excluded for ^{72,74}Ni [80]. The empirical shell model in spite of the weak N=40 shell gives a straightforward explanation (Fig. 3). Due to the small $2^+ - 0^+$ energy difference, identical to the empirical TBME difference, the seniority v =4, 6^+ state moves below the 8^+ state enabling a fast $E2$ transition [80,103]. It should be noted that the LSSM results (Fig. 8) cannot account for the small E_{2^+}. The reappearance of the isomer in ^{76}Ni, however, is strong evidence for the persistence of the N=50 shell in ^{78}Ni [102].

3.4 The N=4 Plus Intruder Shell: ^{80}Zr - ^{100}Sn - ^{132}Sn

Like its lighter analogue ^{56}Ni one major shell lower, the doubly magic ^{100}Sn jj shell closure divides the $N = 4$ HO shell in two subspaces, the lower consisting of $0g_{9/2}$ and the $N = 3$ intruders $(1p, 0f_{5/2})$ for neutron number N$\leq$50 and the higher $(1d, 0g_{7/2}, 2s_{1/2})$, (gds) in short notation, complemented by the $N = 5$ $0h_{11/2}$ intruder for N$\geq$50. Restrictive vertical truncation has to be applied even for the most powerful codes, therefore the most common interactions listed below are given with their respective model space.

In the lower part of the shell a number of empirical interactions were derived for the $\pi\nu(1p_{1/2}, 0g_{9/2})$ [18,19], the $\pi(1p_{1/2}$,$0g_{9/2})$ [20,115] and the

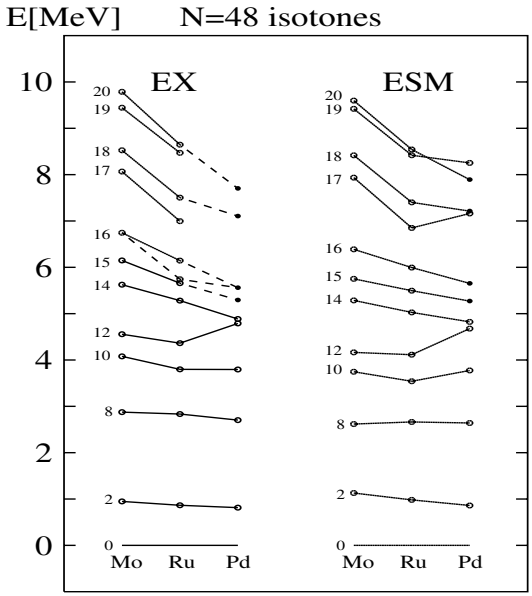

Fig. 9. Experimental and ESM yrast level systematics for N=48 isotones

$\pi(0f_{5/2}, 1p, 0g_{9/2})$ [116] model spaces. Realistic interactions were developed for the $\pi\nu(0f_{5/2}, 1p, 0g_{9/2})$ [40] and the $\pi(0f_{5/2}, 1p, 0g_{9/2})$ [117] subspaces. In the upper part of the shell above N=50 empirical [118,119] and realistic [120,121] interactions were derived for the $\pi(1p_{1/2}, 0g_{9/2})$ ν $(gds, 0h_{11/2})$ subspace, which properly scaled (Sect. 3.5) can be employed below ^{132}Sn, too. To include neutron core excitations across N=50 the lower shell empirical interactions have been extended by the remaining (gds) orbits [122], and a very successful set of realistic TBME was determined for the $\pi\nu(gds)$ model space [77].

The empirical interactions were shown to work extremely well for level and binding energies in the $\pi\nu(1p_{1/2}, 0g_{9/2})$ model space [87,123]. As an example in Fig. 9 experimental and ESM level systematics for N=48 isotones are compared [124]. The agreement in the pattern for known experimental data is so striking that the ESM may be used as a spectroscopic tool for spin-parity assignments in more exotic nuclei [124]. In a close-up view the ESM exhibits the deficiencies discussed in Sect. 2 and towards the end of the model space at high spin large deviations occur even for level energies. A very sensitive probe for interaction and configuration space limitation are high-spin yrast traps, which were abundantly predicted [125] for the $\pi\nu(1p_{1/2}, 0g_{9/2})$ space due to the large overlap and strong $\pi\nu$ interaction in high-spin configurations. Only recently many of them were experimentally identified in N$\leq$50 Pd [126, 127], Ag [124,128,129] and Cd [85] isotopes. As an example the β-decaying record spin I^{π}=21^{+} isomer in ^{94}Ag is chosen [124,128] (see also Sect. 9.2 of

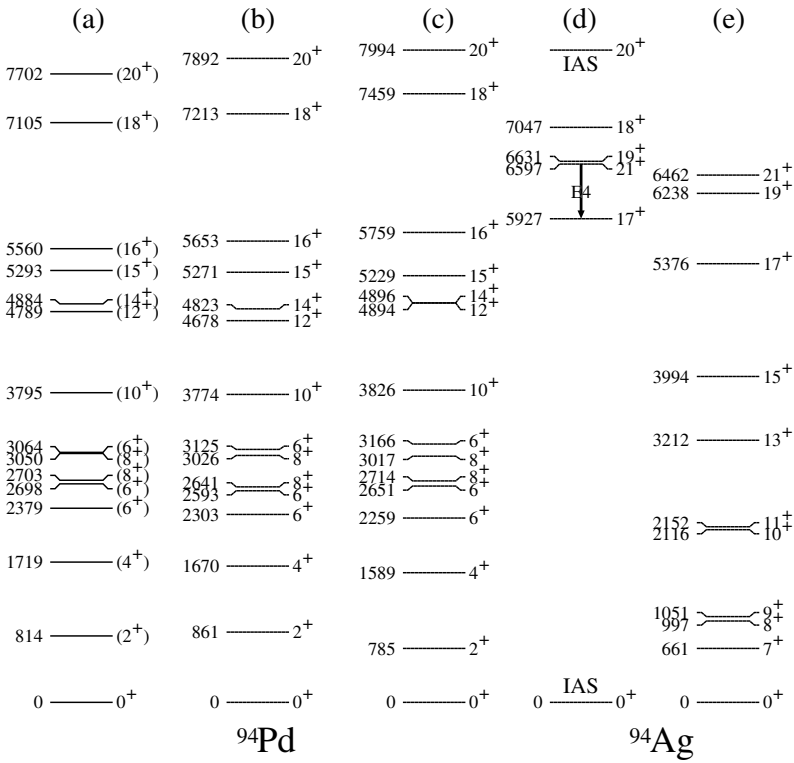

Fig. 10. Experimental levels in ^{94}Pd (**a**) compared to ESM calculations (**b**) and LSSM results (**c**). Selected $T = 0$ and $T = 1$ states in ^{94}Ag from LSSM (**d**) and ESM (**e**). Note the $I = 0, 20$ isobaric analogue states (**c,d**)

[38] in this volume). In Fig. 10 the isomeric parent states in ^{94}Ag and the daughter states in ^{94}Pd are compared to ESM and LSSM results. The ESM works generally well but fails to predict the isomerism of the 21^+ state , which has the highest possible spin in the $(1p_{1/2}, 0g_{9/2})$ model space. The LSSM in the $\pi\nu(gds)$ space including up to $4p4h$ excitations of the ^{100}Sn core (t=4) reproduces the isomerism [124]. As mentioned in Sect. 1.3 the ESM will not be able to account for the dominating $\pi g_{9/2} \rightarrow \nu g_{7/2}$ part of the GT distribution [78] as only the diagonal $\pi g_{9/2} \rightarrow \nu g_{9/2}$ conversion belongs to the model space. Hence severe renormalisation is required [123, 124], whereas the LSSM in the (gds) space will fully account for the GT decay.

To further investigate the rôle of core excitations ^{100}Sn and its neighbours ^{102}Sn and ^{98}Cd provide the appropriate test ground. In Fig. 11 the LSSM results for E_{2^+} and some characteristic $B(E2)$ values in $^{100-104}$Sn and the corresponding Ni isotopes are shown with their dependence on the truncation

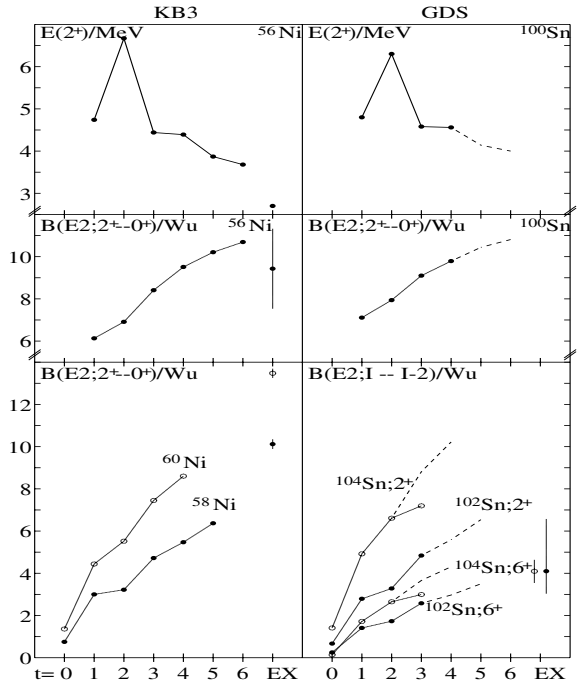

Fig. 11. Convergence of selected observables with truncation level t in the ^{56}Ni and ^{100}Sn *CS* and neighbours in comparison to experiment [77]

level t and compared to experimental data. The (*gds*) space and interaction are used with polarisation charges $\delta e_{\pi,\nu} = 0.5\ e$ [77]. The analogy between the two N=Z shell closures is striking, so that the convergence behaviour with t can be extrapolated from ^{56}Ni to ^{100}Sn, where the computational limit is t=4. As mentioned in Sect. 3.2, t=7-8 would be appropriate for both regions to reach convergence for the *collective* I^π=2^+ observables, while the I^π=6^+ isomeric $E2$ decay strengths [130,131] are already reproduced at t=4. It should be noticed for ^{58,60}Ni and ^{102,104}Sn that truncation to the valence configurations above ^{100}Sn (t=0) requires an unreasonably large polarisation charge of $\delta e_\nu \geq 1.5\ e$ [103,130]. In the two-proton hole nucleus ^{98}Cd the LSSM calculation at t=4 accounts for the $8^+ \rightarrow 6^+$ $E2$ strength and a newly identified core excited I^π=12^+ isomer [85] as predicted and shown in Fig. 5.

The LSSM results on $E2$ strengths open an interesting insight into the microscopic nature of *ph* excitations and effective charges. In Sect. 2.1 it was shown that in a single-j shell all $E2$ matrix elements are proportional to each other, e.g. for the $g^8_{9/2}$ configuration in ^{98}Cd $B(E2;8 \rightarrow 6)$:$B(E2;6 \rightarrow 4)$:$Q^2(8) = 1\ :\ 2.50\ :\ 38.3$. The LSSM results preserve these ratios at all levels of truncation within ∼1 %. This supports the idea of valence nucleons "dressed" by *ph* excitations and the concept of an effective charge. Another

interesting result can be inferred from the comparison of the t=0 and t=4 $B(E2; I_{max} \rightarrow I_{max}-2)$ values for the proton and neutron valence nuclei ^{98}Cd ($I_{max}=8$) and ^{102}Sn ($I_{max}=6$), commonly believed to have rather pure configurations and to be well converged at t=4 (Fig. 11 and [85]). The apparent theoretical polarisation charges are $\delta e_\pi = 0.86\ e$ and $\delta e_\nu = 1.70\ e$. The large isovector effect is due to the empirical fact that valence protons (neutrons) are mainly polarised by neutron (proton) core excitation as can be inferred from inspection of the wave functions. The extracted values agree with the empirical ratio $\delta e_\nu \simeq 2\delta e_\pi$ found for CS nuclei ^{90}Zr [132], ^{132}Sn [133], ^{146}Gd [69] and ^{208}Pb [68] assuming pure valence configurations.

In the Z≤50, 50<N≤54 region numerous shell model calculations were performed with various interactions [118,119,121] for Pd-Sn isotopes and in spite of drastic truncation good agreement was found for the spectroscopy using properly renormalised operators. Typical examples are high-spin states in ^{104}Sn [131], $^{102-104}$In [134], ^{100}Cd [135], ^{99}Cd and ^{101}In [121], which include core excitations, and the GT β-decay of ^{100}In [136] and ^{97,98}Ag [137,138] (see also Sect. 7.2 of [38] in this volume).

Towards ^{132}Sn calculations were performed for the neutron-rich Sn [139] and In [140] isotopes. Recently in the region of astrophysical importance for the r-process Z<50, N≤82 β-decay rates were calculated in the $\pi(1p_{1/2}, 0g_{9/2})$ $\nu(gds, 0h_{11/2})$ space [141] (see Sect. 7.1 of [97]). With the increasing capability of LSSM codes and experimental progress this region will soon be in the center of interest.

3.5 The N=5 Plus Intruder Shell: ^{132}Sn - ^{146}Gd - ^{208}Pb

This region is still inaccessible for LSSM calculations except for semi-magic and $CS \pm 2$ nuclei close to ^{132}Sn and ^{208}Pb. It therefore has been and still is the domain for the ESM approach though realistic interactions are at hand for ^{208}Pb [142] and ^{132}Sn [120,143]. Empirical TBME were extracted from the neighbours of ^{208}Pb, ^{132}Sn and ^{146}Gd, which at Z=64, N=82 shows features of a doubly magic nucleus [144]. The problems arising from incomplete experimental information on two-particle multiplets are greatly alleviated by an empirical rule that relates diagonal TBME from different CS regions to each other [73,145]. For stretched $J_{max} = j_1 + j_2$ and anti-stretched $J_{min} = |j_1 - j_2|$ states in a multiplet

$$TBME(N_1 l_1 j_1, N_2 l_2 j_2, J) =$$

$$\left(\frac{A_{N\pm1}}{A_N}\right)^{1/3} TBME(N_1 \pm 1 l_1 \pm 1 j_1 \pm 1, N_2 \pm 1 l_2 \pm 1 j_2 \pm 1, J') \qquad (19)$$

with N, l, j labelling major HO shell quantum number, orbital and total angular momentum of the orbitals and $J = J_{min}, J_{max}$, $J' = J_{min}, J_{max} \pm 2$. This requests that the respective radial wave functions have the same number of nodes. The scaling factor takes care of the A-dependent different extension

of the radial part of the TBME. As $J_{max,min}$ are different for the two shells for intermediate J values an interpolation may be performed according to the classical angle enclosed by j_1 and j_2 [5] as defined by:

$$\cos\Theta_{12} = \frac{J(J+1) - j_1(j_1+1) - j_2(j_2+1)}{2[j_1(j_1+1)j_2(j_2+1)]^{1/2}} \tag{20}$$

A refined version of this interpolation accounts for the odd-even staggering of TBME [51,146] and performs the procedure for J-even and J-odd states separately. As TBME for the experimentally well known neighbours of ^{208}Pb are at hand the above relation has proven to be extremely useful for ESM calculations around ^{146}Gd [69] (including $L = 3$ phonon coupling, see also Sect. 3.6) and ^{132}Sn [145]. As an example for (19) the $\pi 0h_{9/2}\nu 1g_{9/2}$ multiplet of ^{218}Bi (Fig. 6) can be related to the experimentally incomplete $\pi 0g_{7/2}\nu 1f_{7/2}$ states in ^{134}Sb [147].

3.6 The Z=82-126 Shell: Beyond ^{208}Pb

The nucleus ^{208}Pb is known from numerous experimental and shell model studies as the most stable doubly-magic nucleus. It also is the heaviest CS nucleus. Due to the large number of high-spin orbitals only highly truncated (both *vertical* in the number of orbitals and *horizontal* in their occupation) shell model calculations are possible. These are restricted to isotopic or isotonic chains [148–150] or to the closest neighbours of ^{208}Pb [151]. On the other hand realistic interactions are at hand [142,149,150], which empirically corrected account well for the spectroscopy of nuclei accessible to calculations [150,151]. The ESM was widely used to describe high-spin yrast sequences and isomerism with good success for level energies [68,152,153] (Figs. 4 and 6) and, of course, large corrections to effective one-body operators [68].

Elaborate versions of the shell model include pairing [84] and octupole correlations [152]. The coupling of the $L = 3$ mode based on the $I^\pi = 3^-$ state in ^{208}Pb to high-spin configurations explains the structural features of yrast isomers close to the Z=82 and N=126 lines [152,154–157]. The microscopic structure of collective states in ^{208}Pb was investigated recently in a LSSM study using a realistic interaction [158] in the $2p2h$ model space including 24 orbitals [159].

The merit of modern shell model codes like NATHAN was demonstrated for the N=126 isotones *Po* - *Pu* [54]. The full proton space Z=82-126 comprising 6 orbitals with no truncation applied up to Z=91 (*Pa*) was used together with a realistic interaction [142,151]. The neglect of *ph* degrees of freedom, however, does not allow the description of $L = 3$ correlations. In spite of this vertical truncation, g.s. binding energies, yrast level sequences, $E2$ and pairing properties are excellently reproduced. In Fig. 12a the binding energy differences between theory and experiment are shown, which indicate high predictive power for nuclei beyond Z=90 (*Th*). The level schemes for all

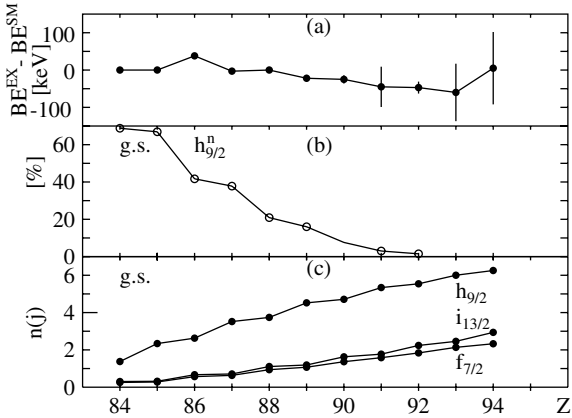

Fig. 12. Binding energy difference to experiment (**a**), partition of the $h^n_{9/2}$ configuration (n =Z-82) (**b**), and occupation of the $h_{9/2}$, $f_{7/2}$ and $i_{13/2}$ orbitals (**c**) in N=126 isotones

known isotones between Po and Th are in excellent agreement with experiment (Fig. 13). The increasing 2^+ energies indicate pairing correlations in the g.s. due to pair scattering from the $0h_{9/2}$ to the $1f_{7/2}$ and $0i_{13/2}$ orbitals. This is borne out in the occupation of these orbitals (Fig. 12b,c), yielding less than 6 protons in the lowest $0h_{9/2}$ orbital at the predicted subshell closure [160] in ^{218}U, and only 5% of the $0h^{10}_{9/2}$ configuration. As the protons are scattered in $L = 0$ pairs seniority is a good quantum number and provides an efficient truncation scheme beyond Z=91 [54]. The delayed filling of the $0h_{9/2}$ orbit distorts the typical pattern of the $B(E2)$ values between the $0h^n_{9/2}$ 8^+ and 6^+ states, which should look as shown in Fig. 2b. The experimental values exhibit a delayed minimum corresponding to the half-filled orbit, which is well reproduced by the calculation. Polarisation charges of $\delta e = 0.5\ e$ were sufficient in contrast to to the ESM requiring $\delta e \simeq 1.0\ e$ [68,133]. As expected the lowest 3^- level is not accounted for in this model space but rather the 3^-_2 state as seen in ^{210}Po (Fig. 13). In summary this first successful LSSM approach in the N=126, Z=82-126 shell gives a promising perspectives for moving into the N>126 shell.

4 Quadrupole Deformation in Light and Medium-Heavy Nuclei

Since the SU(3) approach by Elliot and Flowers to $(1s, 0d)$ shell nuclei [161] the rigorous mapping of deformed states onto spherical shell model configurations was never persued in a satisfactory way. The now available LSSM codes allow at least for an empirical proof that this is possible for nuclei up to A=60. The mapping is limited to quadrupole degrees of freedom excluding

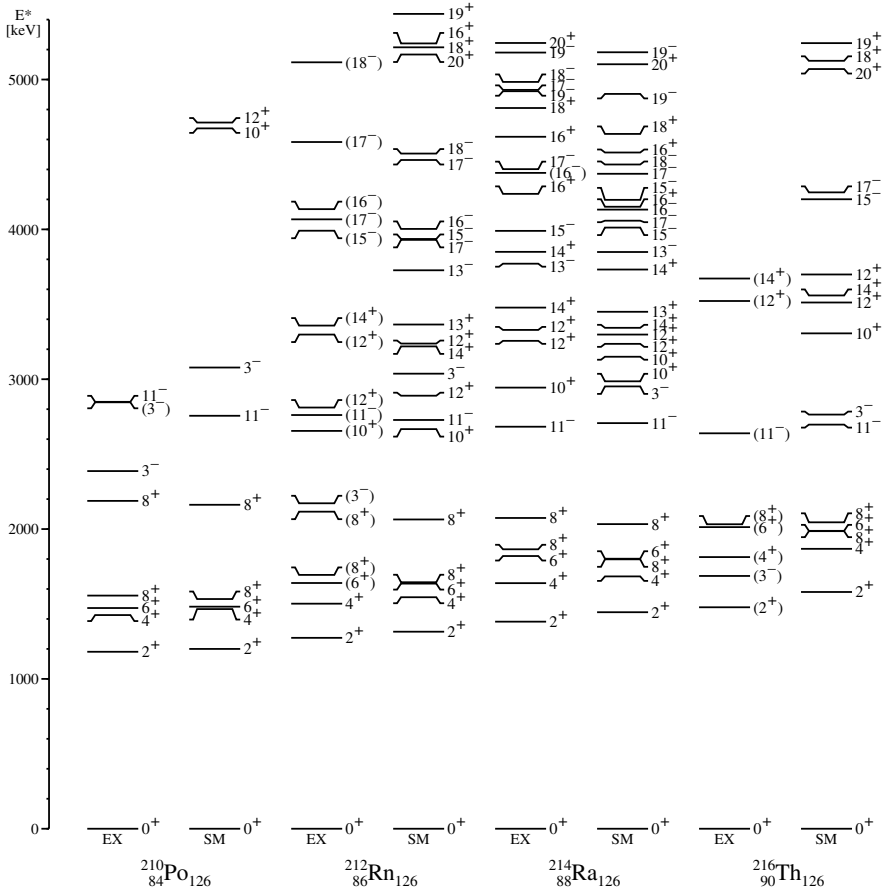

Fig. 13. Experimental and shell model levels for the N=126 isotones of the elements *Po* to *Th*

superdeformation and octupole correlations as these involve more than one major shell.

4.1 The 1s,0d,0f Shell: ^{24}Mg and ^{32}Mg

The $(1s, 0d)$ shell provides a small and tractable model space to study the evolution of deformation. Its maximum is observed at N=Z around the middle of the $0d_{5/2}$ shell in ^{24}Mg, where protons and neutrons, with respect to number, shell occupation, spatial overlap and the strongly binding $T = 0$ part of the TBME, interact in the most efficient way. In Fig. 14 the experimental ^{24}Mg level scheme is compared to shell model results obtained by using different *vertical* truncation levels, namely pure $0d_{5/2}^8$, $(0d_{5/2}, 1s_{1/2})^8$

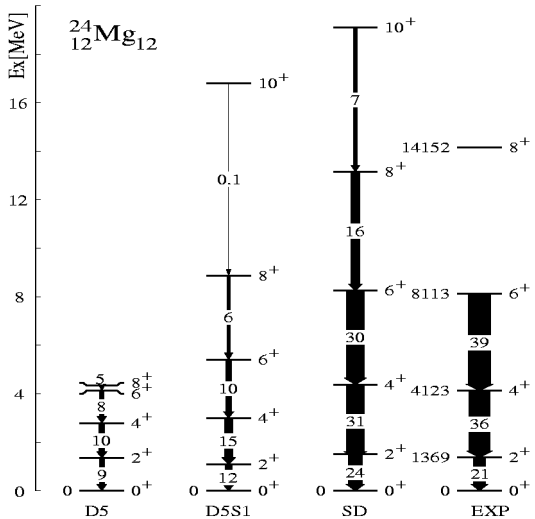

Fig. 14. Experimental results for the g.s. rotational band in ^{24}Mg, in comparison to shell model predictions obtained under the truncation conditions of pure $0d_{5/2}^8$, $(0d_{5/2}, 1s_{1/2})^8$ and full $(1s, 0d)^8$, which are characterised as D5, D5S1 and SD, respectively. The arrow widths give the $B(E2)$ values in W.u. as calculated with polarisation charges $\delta e_{\pi\nu} = 0.5\ e$

and full $(1s, 0d)$ shell. It is obvious that within $0d_{5/2}^8$ the typical rotational behaviour of excitation energies

$$E_I = \frac{\hbar^2}{2\mathcal{J}} I(I+1) \tag{21}$$

with spin I and moment of inertia $\mathcal{J}$ cannot be reproduced. Inclusion of $1s_{1/2}$, which is connected to $0d_{5/2}$ by a stretched (and strong) $\Delta l = 2$ $E2$ transition improves the agreement, but full account of the experiment is obtained only in the complete shell. The importance of the $0d_{3/2}$ orbit, which in ^{16}O is $\geq$ 4.2 MeV above the $1s_{1/2}$ level (Fig. 1) increases with filling of the $0d_{5/2}$. As discussed in Sect. 5 the proton-neutron monopole interaction between spin-orbit partners reduces the effective $s_{1/2}$ - $d_{3/2}$ shell gap to $\sim$ 2.5 MeV in ^{40}Ca (Fig. 1) and even less in mid shell (Fig. 16 of [49] in this volume) enabling increased mixing to support the evolution of deformation. Note the band termination as indicated by level compression and reduced $B(E2)$ strength.

Another shape driving phenomenon is observed [162] in chains of semi-magic nuclei such as Sn (Z=50) and Pb (Z=82) isotopes [162–164] culminating at mid shell. It is ascribed to $2p2h$ excitations between adjacent HO shells across the gap, which by coherent superposition of pairing and proton-neutron interaction create low-lying band heads of prolate and oblate shapes, which coexist with the spherical g.s. of a semi- magic nucleus [162]. In heavy

nuclei the phenomenon is not accessible to shell model calculations. Therefore it came as a surprise when the semi-magic N=20 nucleus ^{32}Mg was found to be deformed in its g.s. as measured by an enhanced $2^+ \rightarrow 0^+$ $E2$ transition strength [88]. Clearly this could not be expected in a pure $(1s, 0d)$ shell model. Inclusion of the $0f_{7/2}$ orbit on the other hand can reproduce the experimental result [165]. The underlying mechanism is the reduction of the $\nu 0d_{3/2}$ - $0f_{7/2}$ shell gap upon removal of $\pi 0d_{5/2}$ protons below Z=14 (Sect. 5). As the effect is isospin symmetric the mirror nucleus ^{32}Ca close to the proton dripline should be deformed as well. This is further discussed below in Sect. 5.3 and in Sect. 3.1 of [49] in this volume.

In conclusion, the evolution of deformation always requires, besides maximum number of interacting valence protons and neutrons in mid shell ($n_\pi \cdot n_\nu$ scaling [51]), a shell driving mechanism. Another consequence is due to the spherical - deformed shell model mapping: rotational bands are terminating when the available maximum model space is exhausted.

4.2 The 0f,1p,0g Shell: ^{48}Cr and ^{56}Ni

It is an intriguing question whether the discussed shape phenomena can be carried on to the next HO shell $N = 3$. The N=Z nucleus corresponding to ^{24}Mg is ^{48}Cr, which indeed exhibits a regular rotational band up to $I = 16$. It is nicely reproduced in LSSM calculations regarding the full $N = 3$ shell [166, 167]. In Fig. 15 the angular momentum I is plotted vs. the $I \rightarrow$ I-2 γ-ray transition energy, which is a measure for the rotational frequency ω [168].

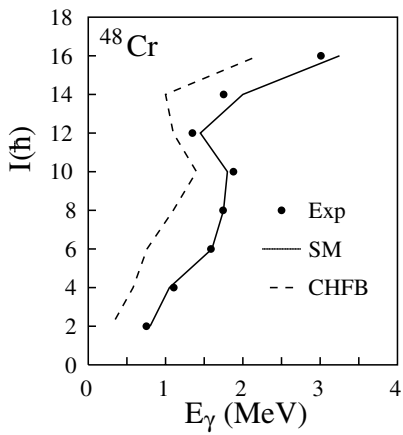

Fig. 15. Angular momentum alignment vs. rotational frequency (γ-ray energy) for the ^{48}Cr g.s. rotational band: experiment vs. shell model (SM) and mean field results (CHFB) [167]

According to (21)

$$\frac{E_\gamma}{2} = \frac{\partial E_I}{\partial I} = \frac{\hbar^2}{\mathcal{J}}(I + 1/2) = \hbar\omega \tag{22}$$

as $I\hbar = \mathcal{J}\omega$ in the classical limit ($I \gg 1$). The backbend at $I = 10$, a typical collective phenomenon of rotational nuclei, which is due to the alignment of a pair of nucleons [168] and the band termination at $I = 16$ are perfectly accounted for. It is the interaction of the stretched $\Delta l = 2$, $f_{7/2}$ - $p_{3/2}$ pair of nucleons that is essential for the collectivity [166] in exact analogy to the $(1s, 0d)$ shell (Sect. 4.1). The rôle of $d_{3/2}$ is taken by $f_{5/2}$ with a corresponding decrease of the $p_{3/2}$ - $f_{5/2}$ gap from ~ 4.0 MeV in ^{40}Ca to ~ 1.0 MeV in ^{56}Ni (Fig. 1) due to filling of the $f_{7/2}$ proton and neutron shell. For comparison the result of a semi-microscopic mean field approach, the cranked shell model [168], is shown, which obviously fails to reproduce the experiment. The deficiency of this model was traced back to the neglect of proton-neutron pairing correlations [169], which are automatically accounted for by the shell model TBME.

The N=40 isotone corresponding to the N=20 ^{32}Mg is ^{66}Fe, where removal of the first two $f_{7/2}$ protons from the Z=28 CS in ^{68}Ni should decrease the $f_{5/2}$ - $g_{9/2}$ gap to enhance $2p2h$ excitations. Rigorous experimental evidence is missing except for the extremely small E_{2^+}=673 keV in ^{66}Fe [111] and the recently assigned deformed shell model quantum numbers to states in the odd-A neighbour ^{67}Fe [170]. A more detailed discussion of the shell driving monopole interaction is given in Sect. 5.

5 Evolution of Shell Structure

The shell structure as discussed and shown in Sect. 1 is not globally fixed for the total Segré chart but subject to change with mass A, neutron excess (N-Z)/A and shell occupation. The dependence on A as discussed in textbooks [42,51] is due to the radial extension of the wave function and characterised by a relative increase in binding for high-l orbitals [42]. Contrary increasing neutron excess due to the softening of the Woods-Saxon shape of the neutron potential causes a relative upward shift of high-l orbitals. This is accompanied by a reduced spin-orbit (SO) splitting [171], which is proportional to the spatial derivative of the central potential. Both scenarios depend smoothly and only weakly on the driving parameters A and N/Z, hence a change of shell structure requires extreme variations of their values. A third scenario based on the monopole shift of selected shell model orbits will be discussed in the following.

5.1 Monopole Shift of SPE

The propagation of SPE throughout a major shell apart from Coulomb effects is governed by the monopole part of the residual interaction [4,36] as defined

by

$$V^m_{jj'} = \sum_J (2J+1)\langle jj'J\,|V|\,jj'J\rangle / \sum_J (2J+1) \tag{23}$$

for a specific multiplet. Single particle energies at a closed shell (CS) and the next higher shell closure (CS') are related by

$$\epsilon^{CS}_j = \epsilon^{CS'}_j + \sum_{j'} (2j'+1-\delta_{jj'}) V^m_{jj'} \tag{24}$$

where j, j' specify in short notation radial, orbital angular momentum, spin and isospin quantum numbers of the nucleons and the sum runs over all orbitals in the major shell. The Kronecker symbol takes care of the Pauli principle for identical nucleons. Particle energies with respect to CS are converted to hole energies in the filled shell CS' by multiplying the r.h.s. of (24) with (-1). Hole energies in CS are transported to hole energies in CS' by using ph TBME to calculate $V^m_{jj'}$ (see Sect. 2.3). The relative shift of two orbitals j_1, j_2 when filling an orbit j' is given by

$$\Delta_{j_1 j_2} = V^m_{j_1 j'}(2j'+1-\delta_{j_1 j'}) - V^m_{j_2 j'}(2j'+1-\delta_{j_2 j'}) \tag{25}$$

Experimentally large monopole shifts are observed in N=29 and 51 isotones and Z=29 (Cu) and 51 (Sb) isotopes. This is demonstrated in Fig. 16 a-d for the proton-neutron and spin-flip combinations $(j_1 j') = (\nu f_{5/2}\pi f_{7/2})$, $(\pi f_{5/2}\nu g_{9/2})$, $(\nu g_{7/2}\pi g_{9/2})$, and $(\pi g_{7/2}\nu h_{11/2})$, respectively [104]. The origin for these exceptional shifts can be traced back to the $(\sigma\cdot\sigma)(\tau\cdot\tau)$ and/or the tensor $(\sigma\times\vec{r})\cdot(\sigma\times\vec{r})(\tau\cdot\tau)$ parts of the in-medium NN interaction [172,173]. They generate strong binding between proton-neutron ($\pi\nu$) spin-orbit partners ($\Delta l = 0, S = 0$) and ($\Delta j = 2, \Delta l = 1, S = 0$) ($\pi\nu$) pairs of nucleons. In Fig. 17 the monopoles V^m for the multiplets relevant for the drastic shifts in Fig. 16 are shown for various realistic and empirically corrected interactions. The dominant rôle of the $S = 0(\uparrow\downarrow)$, $\pi\nu$ ($T = 0$) configurations is clearly prominent. An additional empirical criterion for V^m to be strong requires identical number of nodes in the radial wave functions of the two orbits, i.e. good radial overlap as demanded by the short-range character of the NN interaction.

5.2 Shell Quenching and Stabilisation at N $\gg$ Z

Based on this criterium, and considering $S = 0$, $\Delta l = 0, 1$ pairs to be dominant, the following shell changing scenario develops when proceeding from a N=Z doubly magic nucleus as e.g. ^{16}O, ^{40}Ca along an isotonic chain to N$\gg$Z (see insert in Fig. 18):

- Removing protons from a filled ($\pi n, l, j_< = l-1/2$) orbit, e.g. $0p_{1/2}$, $0d_{3/2}$, in a closed shell (CS) will shift the neutron ($\nu n, l+1, j_> = l+3/2$) orbit,

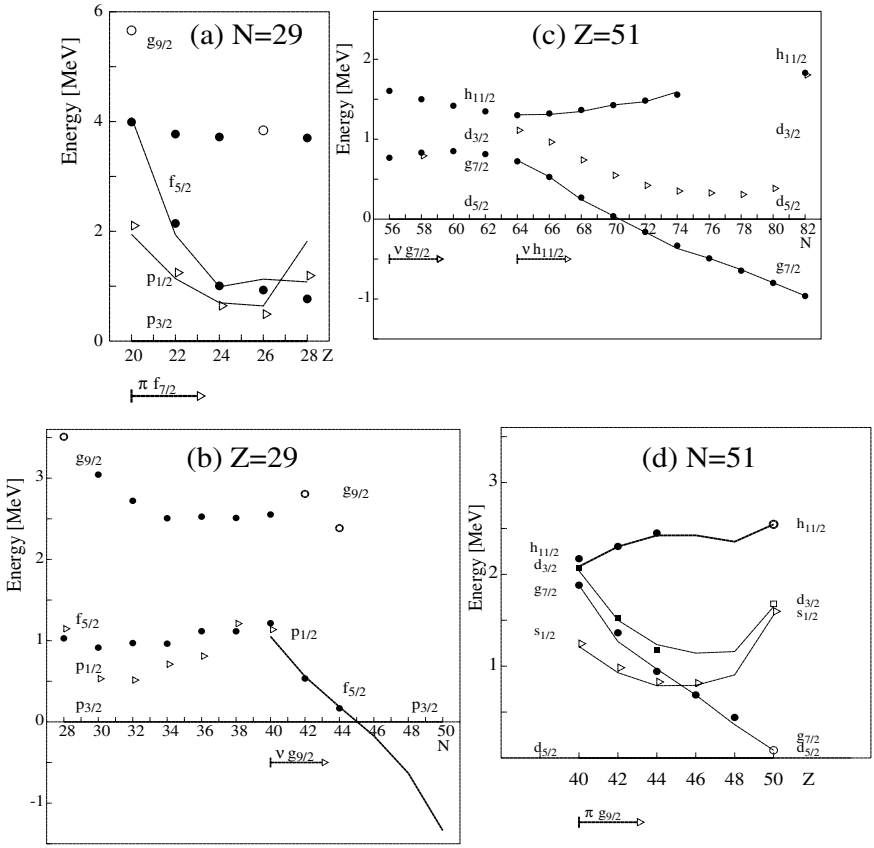

Fig. 16. Monopole shift in N=29 (**a**) and N=51 (**d**) isotones and in Z=29 (Cu) (**b**) and Z=51 (Sb) (**c**)isotopes relative to the reference states $\nu 1p_{3/2}$, $\pi 1p_{3/2}$, $\pi 1d_{5/2}$ and $\nu 1d_{5/2}$, respectively. The lines are results of shell model calculations. The filling of the relevant partner orbits in the extreme single particle model is indicated by arrows. Open circles indicate states not firmly assigned

as e.g. $0d_{5/2}$, $0f_{7/2}$, upward as its binding is weakened relative to the neighbouring orbits as a consequence of the tensor force. This stabilises the shell (as in ^{14}C, ^{36}S, ^{34}Si) and may rearrange the orbitals beyond the closed shell (CS), as observed in ^{15}C.

- On further removal of protons from the next lower lying orbit ($\pi n, l, j_> = l+1/2$), e.g. $0p_{3/2}$, $0d_{5/2}$, its spin-orbit neutron partner $j_<$ will be released in a dramatic way due to the $\sigma\tau$ force to create a new shell CS'.

The effect can be summarised as shown in Fig. 18. A harmonic oscillator (HO) shell closure with magic number $N_m = 8, 20, 40$ changes to $N_m - 2\cdot N = 6, 16(14), 34(32)$, with N counting the HO quanta. The ambiguity for $N > 1$ is due to the presence of $j = 1/2$ orbits as e.g. $s_{1/2}$ or $p_{1/2}$. Trivially in

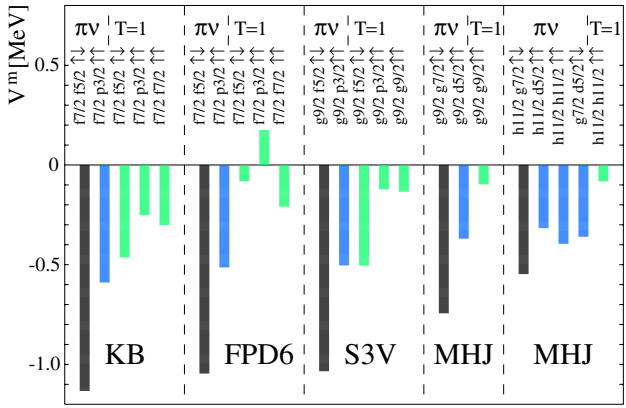

Fig. 17. The monopole part V^m of various realistic and empirically adjusted interactions KB [31], FPD6 [21], S3V [40] and MHJ [143] for selected $\pi\pi$, $\nu\nu$ ($T = 1$) and $\pi\nu$ S =0 ($\uparrow\downarrow$) and 1 ($\uparrow\uparrow$) configurations

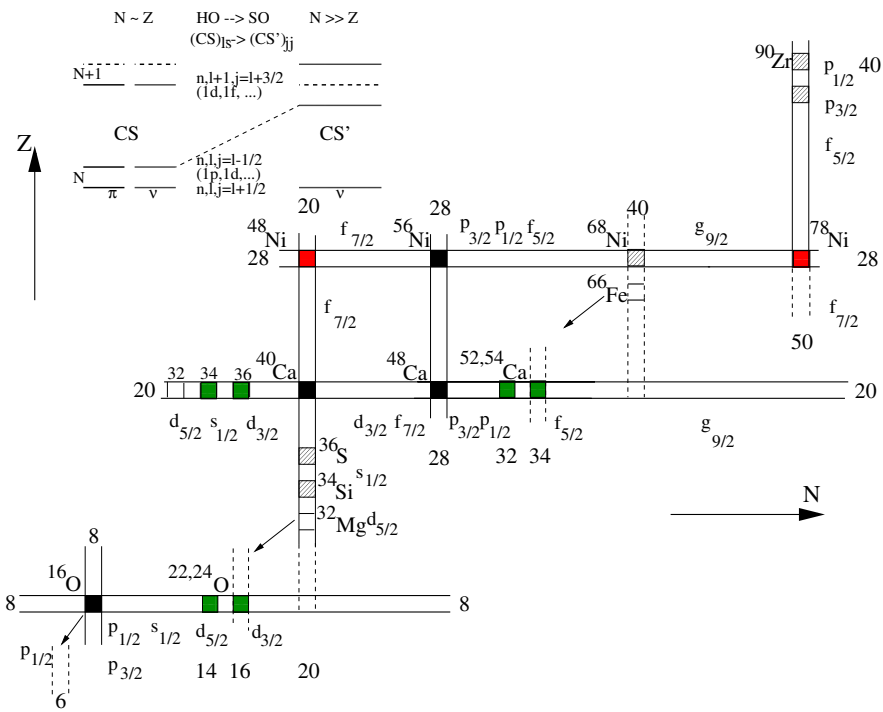

Fig. 18. Schematic chart of known and expected new shell structure in N≫Z nuclei. The insert illustrates the scenario moving from N∼Z to N≫Z along isotonic chains

these shells an I^π=2^+ state cannot be built by recoupling but requires *ph* excitations at the expense of a higher excitation energy. Moreover, the $T = 1$, j^2, $J = 0$ TBME for $j = 1/2$ is identical to V^m_{jj} and always strongly binding and therefore in the evolution of the single particle energy ϵ_j (24) adds a downward shift openening a gap when filling the $j = 1/2$ orbit. This is shown for the $(1s, 0d)$ shell in Fig. 16 of [49] in this volume as taken from [105,172]. The scenario is characterised by the following signature, which substantially deviates from the mechanisms described in the introduction to this section:
• a HO (ls-closed) shell changes to a SO (jj-closed) shell;
• the change is rapid with subshell occupation, and highly localized;
• the scenario is symmetric in isospin projection T_z;
• upon removal of protons the apparent SO splitting between the neutron $l, j_<$ and $j_>$ SO partners due to the $\sigma\tau$ interaction is *increased*;
• contrary in the adjacent HO shell $N + 1$ the SO splitting between the $l, j_>$ and $j_<$ is *decreased* due to the tensor force.

The latter signature is easily verified in Fig. 16 for the two ways towards N≫Z. Removing $f_{7/2}$ ($g_{9/2}$) protons from ^{56}Ni (^{100}Sn) releases the $f_{5/2}$ ($g_{7/2}$) neutrons, which increases the neutron $f(g)$ SO splitting (Fig. 16 a,d), respectively. On the other hand, adding $g_{9/2}$ ($h_{11/2}$) neutrons decreases the SO splitting of proton $f(g)$ orbits (Fig. 16 b,c), respectively. Note that in Fig. 16 only the $j_<$ is shown relative to the adjacent orbits as the $j_>$ partners are lying below the large shell gaps.

The facts that the proton-neutron monopole is always binding (Fig. 17) and that high-spin proton orbitals according to (24,25) are most effective in producing large shifts when progressing from a CS nucleus towards N≫Z by removing protons allow interesting conclusions on possible shell quenching and/or stabilisation.

An indispensable prerequisite to generate a shell rearrangement by monopole interaction is therefore a $\pi j_>$ ($j_<$) that is emptied, which causes a $\nu j'_<$ ($j'_>$) level from below the neutron shell to move up into the shell gap. The opposite scenario, a neutron level moving down from above the shell, is not possible.

Such effective $\pi\nu$ pairs are $\pi p_{3/2}\nu p_{1/2}$ to change N=8 into 6 below ^{16}O, $\pi d_{5/2}\nu d_{3/2}$ to change N=20 into 16(14) below ^{40}Ca, $\pi f_{7/2}\nu f_{5/2}$ to change N=40 into 34(32) below ^{68}Ni and $\pi f_{5/2}\nu g_{9/2}$ above ^{78}Ni. The latter is due to the "low-spin" $\pi f_{5/2}$ and the "A-scaling" of TBME not being effective enough to quench the N=50 shell in ^{78}Ni. This is obviously valid for heavier nuclei, too, $\pi g_{7/2}\nu h_{11/2}$ at N=82 above ^{132}Sn and $\pi h_{9/2}\nu i_{13/2}$ at N=126 above ^{208}Pb (see Fig. 1), as both are good CS nuclei. Ineffective in this sense are the pairs $\pi g_{9/2}\nu g_{7/2}$ along N=82 below ^{132}Sn and $\pi h_{11/2}\nu h_{9/2}$ along N=126 below ^{208}Pb as the neutron levels are lying too deep in the shell (Fig. 1). Therefore the shell quenching invoked to explain r-process abundances [140] must be of different origin, such as the scenario mentioned in the introduction to Sect. 5.

5.3 Experimental Evidence for N=6, 16(14) and 34(32) Shells

The scenario described in Sect. 5.2 accounts in a straightforward way for the recently established new shell effects in light and medium-heavy nuclei, which will be briefly reviewed in the following. Besides single particle states, two-nucleon separation energies S_{2n} and S_{2p} and their differences δ_{2n} and δ_{2p}, respectively, excitation energies E_{2^+} of $I^\pi = 2^+$ states and $B(E2; 2^+ \rightarrow 0^+)$ will be used as signatures for shell structure [13].

In Fig. 19 the evolution of the N=8 shell gap is illustrated. Removal of the $\pi p_{1/2}$ protons from the doubly magic ^{16}O releases the $\nu d_{5/2}$, $S = 0$ partner neutron and hence the $I^\pi = 5/2^+$ and $1/2^+$ levels swap positions from ^{17}O to ^{15}C. The neutron shell gap is preserved in ^{14}C as documented by the large E_{2^+} (Fig. 20a), which is only marginally smaller than in ^{16}O. This demonstrates the aforementioned ambiguity of shell signature for nuclei separated by a $j = 1/2$ subshell (see below), which can build 2^+ states only by *ph* excitations. The dramatic decrease of E_{2^+} observed for ^{12}Be (Fig. 20a) indicates that the removal of the first pair of $\pi p_{3/2}$ protons causes an upward shift of the $\nu p_{1/2}$ spin-flip partner level, thus closing the N=8 gap while opening a N=6 gap. This is impressively corroborated by the ^{11}Be level scheme shown in Fig. 19 and the inversion of the I^π=$1/2^+$ and $1/2^-$ levels. For ^{8}He an estimate for the N=6 shell gap can be inferred from the measured [174] energy difference of the

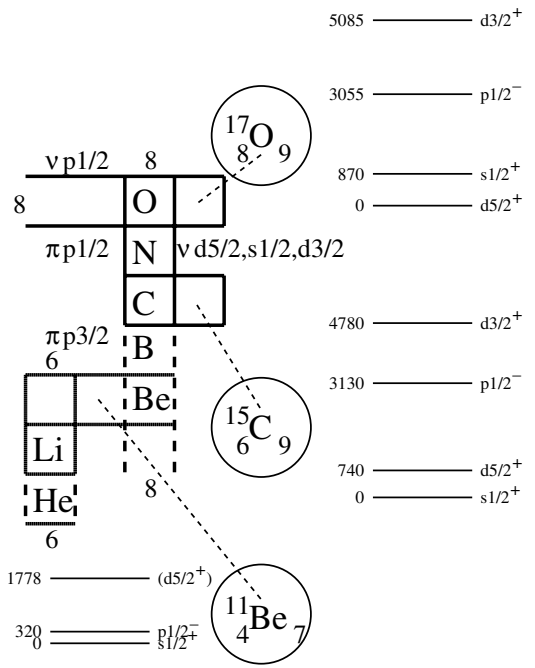

Fig. 19. Experimental evidence for the N=8 to N=6 shell change (see text)

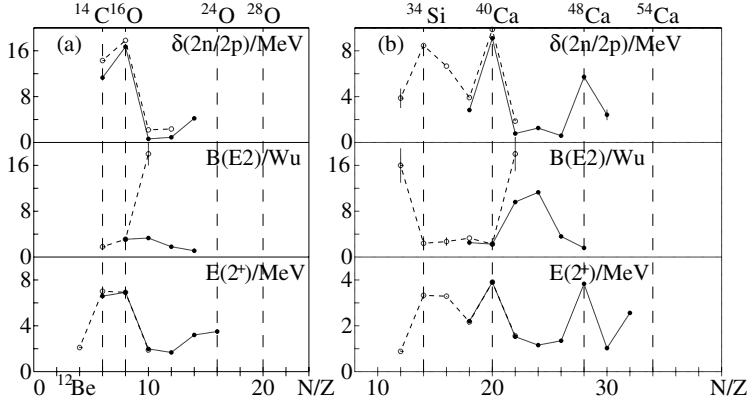

Fig. 20. Shell signatures $\delta_{2n/2p}$, $B(E2;2^+ \rightarrow 0^+)$ and E_{2^+} for shell change between N=8 and 20 along (**a**) Z=8 (O) isotopes (full line) and N=8 isotones (dashed) and (**b**) N=20 isotones (dashed) and Z= 20 (Ca) isotopes (full line)

I^π=3/2$^-$; $\nu p^3_{3/2}$ hole and the I^π=1/2$^-$; $\nu p^2_{3/2} p_{1/2}$ particle states. Using the two-body matrix elements (TBME) from [16] a shell gap $\epsilon(p_{1/2}) - \epsilon(p_{3/2})$= 4.25 MeV is calculated. The N=6 shell stabilisation makes ^{9}Li a good core for ^{11}Li halo calculations (see Sect. 2.2 of [175] in this volume).

One major shell above N=8, the removal of $\pi d_{3/2}$ protons from ^{40}Ca stabilizes the N=20 shell gap because the $S = 0$ partner orbital $\nu f_{7/2}$ is shifted upward. Consequently, ^{36}S and ^{34}Si, again separated by a $j = 1/2$ ($s_{1/2}$) orbit, show doubly magic features as documented in Fig. 20b by large δ_{2p}, E_{2^+} and small $B(E2)$. It would be an experimental challenge to prove the present scenario in the mirror nuclei ^{34,36}Ca, which should exhibit identical shell signature. The upward shift of the $\nu f_{7/2}$ orbital with removal of $\pi d_{3/2}$ protons, on the other hand, quenches the N=28 gap below ^{48}Ca, as exhibited in enhanced $B(E2;0^+ \rightarrow 2^+)$ values measured in Coulomb excitation and the absence of shell closure features in ^{44}S [176]. Following the scenario described in Sect. 5.2, further removal of $\pi d_{5/2}$ protons in N=20 isotones will shift the $\nu d_{3/2}$ orbital into the shell gap, and, aided by $2p2h$ excitations, drives ^{32}Mg to deformation [88]. The evolution of the N=16(14) shell below the $\nu d_{3/2}$ orbital is complete in the oxygen isotopes, where ^{22,24}O exhibit large E_{2^+}, small $B(E2)$ and a rise in δ_{2n} (Fig. 20a). In a recent shell model study this was reproduced quantitatively, at the expense, however, of an "ad hoc" correction of the realistic interaction employed [172]. The locality of the change in shell structure discussed in the present scenario was proven in a recent experiment showing a decrease in E_{2^+} from ^{22}O (3.20 MeV) to ^{20}C (1.56 MeV) [177], which is in contrast to the ^{16}O - ^{14}C trend (Fig. 20). This is due to the $\pi p_{1/2}$ removal, which shifts the $\nu d_{5/2}$ level into the N=16(14) gap.

Further and more detailed experimental evidence for the N=8 to 6, the N=20 to 16(14) and the quenching of the N=28 shells is presented in this volume in Sects. 2.1 and 3.1 of [175] and Sects. 3.1 and 3.3 of [49].

The HO closed shell N=40 in ^{68}Ni is weak and isolated and loses its strength at two particles/holes distance [13,109]. Excitation energy E_{2^+} and $B(E2; 0^+ \rightarrow 2^+)$ exhibit shell closure [106], while δ_{2n} does not show any effect [13,109]. Removing $\pi f_{7/2}$ protons from ^{68}Ni (Fig. 18) prompts the $\nu f_{5/2}$ orbit to move into the (small) N=40 shell gap, so that ^{66}Fe shows features of deformation [111]. This was proven recently by assigning the Nilsson configuration $5/2^+[422]$ to the ground state of ^{67}Fe [170] as discussed in Sect. 4.2. Correlated to this upward shift of the $\nu f_{5/2}$ orbit a N=34 gap opens above the $\nu p_{3/2}, p_{1/2}$ levels as also exhibited by the N=29 single particle states at Z=20 (Fig. 16a). The presence of the $p_{1/2}$ orbit introduces the N=34(32) ambiguity. Experimentally a large E_{2^+} is observed in ^{52}Ca [178] and shell gaps are established in the yrast spectrum of the ^{52,54}Ti isotopes [179].

6 Status and Future

The status of, and future challenges to, the nuclear shell model are determined by (i) the development of novel large scale shell model techniques, (ii) the availability of realistic two-body interactions in model spaces beyond $1\hbar\omega$ accounting effectively for three-body effects, and (iii) the experimental request for predictive power in exotic regions of the Segré chart, which will be accessible with the next generation radioactive-beam facilities.

The limitations of the LSSM approach as discussed in Sects. 1.4 and 3 ask for expansion to $\geq 1\hbar\omega$ spaces in order to treat core excitation in CS nuclei, open jj shells, shell evolution, normal and superdeformation and higher order correlations (e.g. $L = 3$), let alone $\Delta N \geq 1$ giant resonances. Obligatory prerequisites for these extensions are the proper treatment of the spurious state problem and an effective interaction consistent in two adjacent major shells.

The advantage of the shell model approach with an effective interaction to account for all kinds of correlations is depreciated by computational limitations. The Monte Carlo shell model (MCSM) provides a viable way out though its application is limited presently to a few key nuclei and phenomena rather than a broad range spectroscopy. The interaction problem is common to both LSSM and MCSM. The mean field approaches like Hartree- Fock (HF), HF+BCS and relativistic mean field (RMF), based on schematic forces and an effective parametrisation of NN data, account for gross properties mass, shape, shell structure and SPE. The advantage of coping with model spaces of several $\hbar\omega$, however, is counteracted by the difficulty to properly account for correlations.

Acknowledgements

The contributions of my collegues from GSI, GANIL, ORNL and EUROBALL to the latest update of experimental results reviewed in this article are gratefully acknowledged. Numerous enjoyable and enlightening discussions with my collegues from shell model theory B.A. Brown, E. Caurier, A. Covello, M. Hjorth-Jensen, F. Nowacki and T. Otsuka and their help with shell model calculations enabled this practitioner's view of nuclear structure.

References

1. O. Haxel, J.H.D. Jensen, H.E. Suess: Phys. Rev. **75**, 1766 (1949)
2. M. Göppert-Mayer: Phys. Rev. **75**, 1969 (1949)
3. I. Talmi, I. Unna: Nucl. Phys. **30**, 280 (1962)
4. A. de Shalit, I. Talmi: Nuclear Shell Theory, Academic Press, New York, 1963
5. P.J. Brussaard, P.W.M. Glaudemans: Shell model applications in nuclear spectroscopy, North-Holland, Amsterdam, 1977
6. B.A. Brown, B.H. Wildenthal: Ann. Rev. of Nucl. Part. Sci. **38**, 29 (1988)
7. A. Poves, A.P. Zuker: Phys. Rep. **70**, 235 (1981)
8. Proc. Int. RIKEN Symposium Shell Model 2000, eds. T. Otsuka, H. Sakurai, I. Tanihata, Nucl. Phys A **704** (2002)
9. G. Martínez-Pinedo: to be published in this series
10. T. Schmidt: Z. Phys. **106**, 358 (1937)
11. M. Göppert-Mayer, J.H.D. Jensen: Elementary Theory of Nuclear Shell Structure, J. Wiley & Sons, New York, 1955
12. P. Möller, J.R. Nix, K.-L. Kratz: At. Data Nucl. Data Tab. **66**, 131 (1997)
13. H. Grawe, M. Lewitowicz: Nucl. Phys. A **693**, 116 (2001)
14. J. Duflo, A.P. Zuker: Phys. Rev. C **59**, 2347 (1999)
15. B.A. Brown: Phys. Rev. C **58**, 220 (1998)
16. B. Cohen, D. Kurath: Nucl. Phys. A **101**, 1 (1967)
17. W. Kutschera, B.A. Brown, K. Ogawa: Riv. Nuovo Cim. **1**, No. 12 (1978)
18. F.J.D. Serduke, R.D. Lawson, D.H. Gloeckner: Nucl. Phys. A **256**, 45 (1976)
19. R. Gross, A. Frenkel: Nucl. Phys. A **267**, 85 (1976)
20. J. Blomqvist, L. Rydström: Phys. Scripta **31**, 31 (1985)
21. W.A. Richter et al.: Nucl. Phys. A **523**, 325 (1991)
22. M. Honma et al.: Phys. Rev. C **69**, 034335 (2004)
23. K. Heyde: The Nuclear Shell Model, Springer, Berlin, 1994
24. S. Arvieu, S.A. Moszkowski: Phys. Rev. **145**, 830 (1966)
25. T.R.H. Skyrme: Nucl. Phys. **9**, 615 and 635 (1959); D. Vautherin and D.M. Brink: Phys. Rev. C **5**, 626 (1972)
26. D. Gogny: Nucl. Phys. A **237**, 399 (1975)
27. R. Machleidt: Adv. Nucl. Phys. **19**, 189 (1989)
28. M. Lacombe et al.: Phys. Rev. C **21**, 861 (1980)
29. V.G.J. Stoks et al.: Phys. Rev. C **49**, 2950 (1994)
30. R.B. Wiringa, V.G.J. Stoks, R. Schiavilla: Phys. Rev. C **51**, 38 (1995)
31. T.T.S. Kuo, G.E. Brown: Nucl. Phys. A **114**, 241 (1968)
32. T.T.S. Kuo, E. Osnes: Springer Lecture Notes of Physics **364**, 1 (190)
33. M. Hjorth-Jensen et al.: Phys. Rep. **261**, 125 (1995)

34. S. Bogner, T.T.S. Kuo, L. Coraggio: Nucl. Phys. A **684**, 432c (2001)
35. Y. Utsono et al.: Phys. Rev. C **60**, 054315 (1999)
36. E. Caurier et al.: Phys. Rev. C **50**, 225 (1994)
37. R. Neugart, G. Neyens: to be published in this series
38. E. Roeckl, Decay Studies of N≃Z Nuclei, Lect. Notes Phys. **651**, 223–261 (2004)
39. N. Severijns, Weak Interaction Studies by Precision Experiments in Nuclear Beta Decay, Lect. Notes Phys. **651**, 339–381 (2004)
40. J. Sinatkas et al.: J. Phys. G **18**, 1377 and 1401 (1992)
41. T. Engeland et al.: Phys. Rev. C **61**, 021302(R) (2000)
42. A. Bohr, B.R. Mottelson: Nuclear Structure, World Scientific, Singapore, 1998
43. I. Hamamoto: Proc. Int. Symp. Nuclear Structure Physics, eds. R. Casten et al., World Scientific, Singapore 2001, p.31
44. B.A. Brown: Nucl. Phys. A **704**, 11c (2002)
45. G. Martínez-Pinedo et al.: Phys. Rev. C **53**, R2602 (1996)
46. I.S. Towner, F.C. Khanna: Nucl. Phys. A **399**, 334 (1983)
47. K.H. Maier et al.: Nucl. Phys. A **183**, 289 (1972)
48. H. Grawe, H.H. Bertschat, H. Haas, Hyperfine Interactions **15/16**, 65 (1983)
49. N. Alamanos, A. Gillibert, Selected Topics in Reaction Studies with Exotic Nuclei, Lect. Notes Phys. **651**, 295–337 (2004)
50. V.F. Weisskopf: Phys. Rev. **83**, 1073 (1951)
51. R.F. Casten: Nuclear Structure from a Simple Perspective, Oxford University Press, 2000
52. P. Navratil, B.R. Barrett: Phys. Rev. C **57**, 3119 (1998)
53. B.R. Barrett, P. Navratil, J.P. Vary: Nucl. Phys. A **704**, 254c (2002)
54. E. Caurier, M. Rejmund, H. Grawe: Phys. Rev. C **67**, 054310 (2003)
55. T. Otsuka et al.: Nucl. Phys. A **704**, 21c (2002)
56. J.B. French, M.H. McFarlane: Nucl. Phys. A **26** ,168 (1961)
57. D. Zwarts: Comp. Phys. Comm. **38**, 365 (1985)
58. M. Hausmann et al.: Phys. Rev. C **68**, 024309 (2003)
59. A. Lisetskiy et al.: Nucl. Phys. A **677**, 100 (2000)
60. R.R. Whitehead et al.: Adv. in Nucl. Phys. **9**, 123 (1977)
61. B.A. Brown et al.: MSU-NSCL Report No. 524 (1985)
62. E. Caurier et al.: Phys. Rev. C **59**, 2033 (1999)
63. E. Caurier, G. Martínez-Pinedo: Nucl. Phys. A **704**, 60c (2002)
64. T. Mizusaki: RIKEN Acc. Progr. Report **33**, 14 (2000)
65. A. Schmidt et al.: Phys. Rev. C **62**, 044319 (2000)
66. C. Mazzocchi et al.: Eur. Phys. J. A **12**, 269 (2001)
67. E. Caurier: private communication
68. J. Blomqvist: Proc. ASHPIN, Argonne, 1979, ANL/PHY-79-4, p.155
69. J. Blomqvist et al.: Z. Phys. A **312**, 27 (1983)
70. T. Ishii et al.: Phys. Rev. Lett. **81**, 39 (2000)
71. A. Amusa, R.D. Lawson: Z. Physik A **307**, 333 (1982)
72. M. Rejmund et al.: Z. Physik A **359**, 243 (1997)
73. J. Blomqvist: CERN Report No. 81-09, CERN, Geneva, 1981, p. 536
74. I.M. Band, Yu. I. Kharitonov: Nucl. Data. Tabl. **10**, 107 (1971)
75. F. Hardemann et al.: Hyperfine Interactions **59**, 13 (1990)
76. H. Grawe et al.: AIP CP **481**, 177 (1999)
77. F. Nowacki: Nucl. Phys. A **704**, 223c (2002) and private communication

78. L. Batist et al.: Nucl. Phys. A **720**, 222 (2003)
79. G. Audi, A.H. Wapstra: Nucl. Phys. A **565**, 1 (1993)
80. M. Sawicka et al.: Phys. Rev. C **68**, 044304 (2003)
81. R. Grzywacz et al.: Phys. Rev. Lett. **81**, 766 (1998)
82. P. Daly et al.: Physica Scripta T **56**, 94 (1995)
83. J.H. McNeill et al.: Phys. Rev. Lett. **63**, 860 (1989)
84. D.J. Decman et al.: Z. Phys. A **310**, 55 (1983)
85. A. Blazhev et al.: Phys. Rev. C **69**, 064304 (2004)
86. S. Franchoo et al.: Phys. Rev. C **69**, 044305 (2004)
87. D. Rudolph, K.P. Lieb, H. Grawe: Nucl. Phys. A **597**, 298 (1996)
88. T. Motobayashi et al.: Phys. Lett. B **346**, 9 (1995)
89. C.E. Svensson et al.: Phys. Rev. Lett. **85**, 2693 (2000)
90. T. Otsuka et al.: Phys. Rev. Lett. **81**, 1588 (1998)
91. G. Martínez-Pinedo et al.: Phys. Rev. C **55**, 187 (1997)
92. S.M. Lenzi: Nucl. Phys. A **704**, 124c (2002)
93. E. Caurier et al.: Nucl. Phys. A **693**, 439 (1999)
94. M. Bentley et al.: Phys. Lett. B **437**, 243 (1998)
95. S.M. Lenzi et al.: Phys. Rev. Lett. **87**, 122501 (2001)
96. A.P. Zuker et al.: Phys. Rev. Lett. **89**, 142502 (2002)
97. K. Langanke, F.-K. Thielemann, M. Wiescher, Nuclear Astrophysics and Nuclei far from Stability, Lect. Notes Phys. **651**, 383–467 (2004)
98. T. Mizusaki et al.: Phys. Rev. C **59**, R1846 (1999)
99. D. Rudolph et al.: Phys. Rev. Lett. **82**, 3763 (1999)
100. D. Rudolph et al.: Phys. Rev. Lett. **80**, 3018 (1998)
101. T. Mizusaki et al.: Nucl. Phys. A **704**, 190c (2002)
102. M. Sawicka et al.: Eur. Phys. J. A **109** (2004)
103. H. Grawe et al.: Nucl. Phys. A **704**, 211c (2002)
104. H. Grawe, Acta Physica Polonica B **34**, 2267 (2003)
105. B.A. Brown: 10th Int. Conf. on Nuclear Reaction Mechanisms, ed. E. Gradioli, Varenna 2003, Ricerca Scientifica ed Educazione Permanente, Suppl. Nr. 122, p. 41 (2003)
106. O. Sorlin et al.: Phys. Rev. Lett. **88**, 092501 (2002)
107. E. Caurier, F. Nowacki, A. Poves: Eur. Phys. J. A **15**, 145 (2002)
108. T. Ishii et al.: Act. Phys. Pol. B **32**, 739 (2001)
109. H. Grawe et al.: Proc. Tours 2000, AIP CP **561**, 287 (2001)
110. G. Georgiev et al.: J. Phys. G **28**, 2993 (2002)
111. M. Hanawald et al.: Phys. Rev. Lett. **82**, 1391 (1999)
112. K.H. Langanke et al.: Phys. Rev. C **67**, 044314 (2003)
113. P.G. Reinhard et al.: RIKEN Review **26**, 23 (2000)
114. O. Kenn et al.: Phys. Rev. C **65**, 034308 (2003)
115. I.P. Johnstone, L.D. Skouras: Eur. Phys. J. A **11**, 125 (2001)
116. X. Ji, B.H. Wildenthal: Phys. Rev. C **37**, 1256 (1988), C **38**, 2849 (1988), C **40**, 389 (1989)
117. L. Coraggio et al.: J. Phys. G **26**, 1697 (2000)
118. H. Grawe et al.: Physica Scripta T **56**, 71 (1995)
119. B.A. Brown, K. Rykaczewski: Phys. Rev. C **50**, R2270 (1994)
120. A. Covello et al.: Acta Phys. Pol. B **34**, 2257 (2002)
121. M. Lipoglavšek et al.: Phys. Rev. C **66**, 011302(R) (2002)
122. I.P. Johnstone, L.D. Skouras: Phys. Rev. C **55**, 1227 (1995)

123. H. Herndl, B.A. Brown: Nucl. Phys. A **627**, 35 (1996)
124. C. Plettner et al.: Nucl. Phys. A **733**, 20 (2004)
125. K. Ogawa: Phys. Rev. C **28**, 958 (1983)
126. E. Nolte, H. Hicks: Phys. Lett. B **97**, 55 (1980)
127. M. Górska et al.: Z. Phys. A **353**, 233 (1995)
128. M. La Commara et al.: Nucl. Phys. A **708**, 167 (2002)
129. J. Döring et al.: Phys. Rev. C **68**, 034306 (2003)
130. M. Lipoglavšek et al.: Phys. Lett. B **440**, 2467 (1998)
131. M. Górska et al.: Phys. Rev. C **58**, 108 (1998)
132. P. Raghavan et al.: Phys. Rev. Lett. **54**, 2592 (1985)
133. J.P. Omtvedt et al.: Phys. Rev. Lett. **75**, 3090 (1995)
134. D. Seweryniak et al.: Nucl. Phys. A **589**, 175 (1995)
135. R.M. Clark et al.: Phys. Rev. C **61**, 044311 (2000)
136. C. Plettner et al.: Phys. Rev. C **66**, 044319 (2002)
137. Z. Hu et al.: Phys. Rev. C **60**, 024315 (1999)
138. Z. Hu et al.: Phys. Rev. C **62**, 064315 (2000)
139. T. Engeland et al.: Proc. 6th Spring Meeting on Nuclear Physics, S. Agata, Italy, 1998, ed. A. Covello, World Scientific, Singapore , 1999, p.117
140. I. Dillmann et al.: Phys. Rev. Lett. **91**, 162503 (2003)
141. G. Martínez-Pinedo, K.H. Langanke: Phys. Rev. Lett. **83**, 4502 (1999)
142. T.T.S. Kuo, G.A. Herling: NRL Memorandum Report, No. 2258 (1971)
143. M. Hjorth-Jensen: private communication
144. M. Ogawa et al.: Phys. Rev. Lett. **41**, 289 (1978)
145. A. Korgul et al.: Eur. Phys. J. A **7**, 167 (2000)
146. J.P. Schiffer: Ann. Phys. **66**, 798 (1971)
147. M.N. Mineva et al.: Eur. Phys. J. A **11**, 9 (2001)
148. D. Zwarts, P.W.M. Glaudemans: Z. Physik A **320**, 487 (1985)
149. L. Coraggio et al.: Phys. Rev. C **58**, 3346 (1998)
150. L. Coraggio et al.: Phys. Rev. C **60**, 064306 (1999)
151. E.K. Warburton, B.A. Brown: C **43**, 602 (1991)
152. S.J. Poletti et al.: Nucl. Phys. A **448**, 189 (1986)
153. K. Hauschild et al.: Phys. Rev. Lett. **87**, 072501 (2001)
154. I. Hamamoto: Phys. Rep. **10**, 63 (1974)
155. M. Rejmund et al.: Eur. Phys. J. A **8**, 161 (2000)
156. B. Fornal et al.: Phys. Rev. Lett. **87**, 212501 (2001)
157. G. Dracoulis et al.: Nucl. Phys. A **493**, 145 (1989)
158. G. Bertsch et al.: Nucl. Phys. A **284**, 399 (1977)
159. B.A. Brown: Phys. Rev. Lett. **85**, 5300 (2000)
160. K. Rutz et al.: Nucl. Phys. A **634**, 67 (1998)
161. J.P. Eliott and B.H. Flowers: Proc. Roy. Soc. A **229**, 536 (1955)
162. J.L. Wood et al.: Phys. Rep. **215**, 101 (1992)
163. J. Heese et al.: Phys. Lett. B **302**, 390 (1993)
164. A.N. Andreyev et al.: Nature **405**, 430 (2000)
165. E. Caurier et al.: Phys. Rev. C **58**, 2033 (1998)
166. E. Caurier et al.: Phys. Rev. Lett. **75**, 2466 (1995)
167. S.M. Lenzi et al.: Z. Phys. A **354**, 117 (1996)
168. R. Wyss: to be published in this series
169. A. Poves, G. Martínez-Pinedo: Phys. Lett. B **430**, 203 (1998)
170. M. Sawicka et al.: Eur. Phys. J. A **16**, 51 (2002)

171. J. Dobaczewski et al.: Phys. Rev. Lett. **72**, 981 (1994)
172. T. Otsuka et al.: Phys. Rev. Lett. **87**, 082502 (2001)
173. T. Otsuka: private communication
174. K. Markenroth et al.: Nucl. Phys. A **679**, 467 (2001)
175. J. Al-Khalili, An Introduction to Halo Nuclei, Lect. Notes Phys. **651**, 77–112 (2004)
176. T. Glasmacher et al.: Phys. Lett. B **395**, 163 (1997)
177. M. Stanoiu et al.: NS2002, Berkeley, AIP CP **656**, 311 (2002)
178. A. Huck et al.: Phys. Rev. C **31**, 2226 (1985)
179. R.V.F. Janssens et al.: Phys. Lett. B **546**, 55 (2002)